

IMBALANCE RESPONSE OF A FOUR DEGREE OF FREEDOM RIGID ROTOR SUPPORTED
BY HYBRID THREE PAD AIR FOIL BEARING

by

PRAJWAL KRISHNA SHETTY

Presented to the Faculty of the Graduate School of
The University of Texas at Arlington in Partial Fulfillment
of the requirements
for the degree of

MASTER OF SCIENCE IN MECHANICAL ENGINEERING

THE UNIVERSITY OF TEXAS AT ARLINGTON
DECEMBER 2010

DEDICATED TO ALMIGHTY AND MY FAMILY

Copyright © by Prajwal Shetty 2010

All Rights Reserved

ACKNOWLEDGEMENTS

I would like to thank my committee chair, Dr. Daejong Kim and Dr. Donghyun Lee for their guidance and support throughout the course of this research. I would also like to thank Dr. Alan Bowling and Dr. Kent Lawrence for obliging to be a part of my thesis defense committee.

I would also like to extend my appreciation to Kermit Beird and Sam Williams from the machine shop for their continuous help and support through the course of my research

My thanks also go to my colleagues at the Microturbomachinery Lab and my friends at The University of Texas at Arlington. I would also like to thank the machinists of UTA for their help in fabrication of the test rig.

November 22, 2010

ABSTRACT

IMBALANCE RESPONSE OF A FOUR DEGREE OF FREEDOM RIGID ROTOR SUPPORTED
BY HYBRID THREE PAD AIR FOIL BEARING

PRAJWAL KRISHNA SHETTY, M.S.

The University of Texas at Arlington, 2010

Supervising Professor: Daejong Kim

Air foil bearings (AFB's) are widely used in small to midsized turbomachinery. They provide safer, cleaner and cheaper bearing operation. They are simple in construction, offer very low drag friction and have very high reliability at high speed operations. A major advantage of air foil bearings compared to conventional rigid surface bearings is their superior dynamic performance in rotor bearing systems. Since there is no contact between the rotor and bearing surface, the air foil bearings have a higher service life compared to rigid surface bearings. Hybrid AFB's operate under both hydrodynamic and hydrostatic condition.

The present study is a continuation of the work on hybrid air foil bearings (HAFB) by Kim and Park, where they develop and present an AFB which operates in hydrodynamic condition in the presence of a hydrostatic lift. Their experiments proved that the HAFB's have greater rotor dynamic performance and load capacity compared to their hydrodynamic counterpart. They also showed that HAFB's have better heat dissipation capacity of the parasitic heat generated due to viscous drag of the rotor and due to conduction from various parts of the test rig, thereby enhancing their performance. Later Manish developed a model to determine the bearing stiffness and damping coefficient using linear perturbation method. He also presented detailed study on

the dependence of stiffness and damping coefficients on various bearing design parameters like supply pressure, feed parameter, excitation frequency and bearing number

This article presents the non linear imbalance response of a four degree of freedom (DOF) rigid rotor supported by two, three pad HAFB's. Generally, imbalance response of a rotor has been performed considering two degrees of freedom i.e. cylindrical mode of vibration. This assumption makes it hard to predict the response of rotor bearing system during failure mode of the bearing, since bearing failure occurs predominantly due to conical vibrations. The translational and gyroscopic motion of the rotor has been determined by solving non linear degrees of motion corresponding to the DOF's. Both hydrodynamic and hydrostatic conditions tests were performed using a custom made test rig. Imbalance response simulations were performed and compared with the empirical results.

TABLE OF CONTENTS

	PAGE
ACKNOWLEDGEMENT.....	iv
ABSTRACT.....	v
LIST OF ILLUSTRATIONS.....	ix
LIST OF TABLES.....	xii
NOMENCLATURE.....	xiii
Chapter	
1. INTRODUCTION.....	1
1.1 Air Foil Bearing.....	1
1.1.1 Principle of Operation.....	2
1.1.2 Introduction to Hybrid Air Foil Bearing.....	4
1.1.3 Configuration of three-pad HAFB.....	5
1.2 Literature Review on Previous Experimental Study.....	7
1.3 Objective of Current Research.....	10
1.4 Summary of Major Contributions.....	11
2. DESCRIPTION OF TEST BEARING AND TEST RIG.....	13
2.1 Design Parameters of Bearing.....	13
2.2 Manufacturing Process of HAFB.....	15
2.3 Description of Test Rig.....	23
3. METHODOLOGY.....	34
3.1 Theory and Governing Equations.....	34
3.2 Experimental Methods.....	39
3.2.1 Baseline Subtraction.....	40
3.2.2 Data Process.....	42

4. RESULTS AND DISCUSSIONS.....	44
4.1 Imbalance Response in Hydrostatic Mode.....	44
4.1.1 Baseline Response.....	44
4.1.2 Cylindrical Mode.....	47
4.1.3 Conical Mode.....	53
5. CONCLUSIONS AND RECOMMENDATIONS.....	57
5.1 Conclusions.....	57
5.2 Recommendations for future work.....	58
APPENDIX	
A. SETUP AND OPERATION OF HAFB AND TEST RIG.....	60
B. METHOD OF ATTACHING ORIFICE TUBE TO THE BEARING.....	66
C. DESCRIPTION OF DIGITAL DATA ACQUISITION AND HARDWARE USED.....	69
D. LIMITATIONS OF DIGITAL FILTER IMPLEMENTED & DETAILS OF NEW FILTER.....	76
BIBLIOGRAPHY.....	80
BIOGRAPHICAL INFORMATION.....	82

LIST OF ILLUSTRATIONS

Figure	Page
1.1 Schematic of a circular top foil, continuous bump air foil bearing showing eccentricity and radial clearance.....	3
1.2 Schematic of a Circular top foil HAFB used by previous researchers.....	5
1.3 Schematic of a HAFB showing preload, set bore clearance and pad configuration.....	6
2.1 Schematic of a three pad HAFB showing top foil and bump foils.....	14
2.2 Bump foil forming jig.....	17
2.3 Heat Treatment for stainless steel 316.....	18
2.4 Corrugated Bump Foil.....	18
2.5 Lower part of the top foil forming jig showing orifice tube slot and locating shims.....	19
2.6 Assembled top foil forming jig.....	20
2.7 Schematic of a bearing sleeve.....	21
2.8 Assembled HAFB.....	22
2.9 Photo of manufactured three-pad foil bearing.....	22
2.10 L Shaped circular cross section orifice tubes.....	23
2.11 General Layout of the test rig.....	25
2.12 Picture of the test facility.....	26
2.13 Motor cooling jacket.....	27
2.14 Assembly of the stator and cooling jacket.....	28
2.15 Mass imbalance grooves on the rotor.....	29
2.16 Rotor.....	30
2.17 Thrust Bearing Assembly.....	32
2.18 Thrust bearing components.....	33

3.1 Rotor bearing system.....	35
3.2 Rotor showing co ordinate system used for analysis.....	35
3.3 Mesh Defined for analysis.....	37
4.1 Residual Baseline imbalance response waterfall plot.....	45
4.2 Raw Data Bode Plot for baseline vibration along horizontal and vertical direction.....	46
4.3 Total In Phase imbalance response waterfall plot.....	48
4.4 Raw Data Bode Plot for cylindrical vibration along horizontal and vertical direction.....	49
4.5 Calibrated in phase response amplitude and phase angle curve.....	50
4.6 Simulation Bode Blot for in phase response.....	51
4.7 Simulation results- Waterfall plot for in phase imbalance response.....	52
4.8 Total out of phase imbalance response waterfall plot.....	54
4.9 Raw Data Speed Vs Amplitude curve for conical vibration along horizontal and vertical direction.....	55
4.10 Calibrated Out of phase imbalance response Bode Plots.....	56
5.1 Front bearing top foil showing rubbing marks at the edges.....	59
A.1 Bearing housing showing shorter leading edge.....	61
A.2 Schematic of the rotor adapter.....	62
A.3 thrust bearing inner housing, spacer and outer housing exploded View.....	64
A.4 Outer housing of the thrust bearing showing air supply holes.....	65
B.1 Top Foils with laser welded orifice tubes showing rubbing marks and protrusion at the air injection area	67
B.2 Front bearing top foil showing crack at the soldered joint.....	68
C.1 Schematic of the components used for Data acquisition.....	70
C.2 Probe to Demodulator Wiring Schematic.....	72
C.3 Probe 1 calibration curve.....	73
C.4 Front Panel view of Labview Data Acquisition system at 34000 RPM running under Baseline condition.....	75

D.1 Filtered signal comparison between the filter used in the article and the new filter designed.....	77
--	----

LIST OF TABLES

Table	Page
2.1 Bearing Parameters used in simulation.....	15
2.2 Specifications of the rotor used for simulation.....	30
4.1 Imbalance mass location and modes of vibration being excited.....	44
C.1 Description of hardware used for Data Acquisition.....	71
C.2 Linear Range Proximity Probe Calibration Data.....	73

NOMENCLATURE

R: Radius of the bearing pad

C_j : Nominal clearance of journal bearing

C: Radial clearance of the circular top foils journal bearing

C_{SB} : Set bore clearance

e: Eccentricity

e_x, e_y : Translational displacement of rotor

F_{X_B}, F_{Y_B} : Forces induced by journal bearings

M_{ξ_B}, M_{ψ_B} : Moments induced by journal bearings

F_{X_U}, F_{Y_U} : Forces induced by imbalance of rotor

h_j : Film thickness of journal bearing

H_j : Nondimensional journal bearing film thickness, $H_j = \frac{h_j}{C_j}$

I_T : Translational moment of inertia

r_p : Bearing preload

R_p : Non Dimensionalized Bearing preload, $R_p = \frac{r_p}{C_j}$

I_p : Polar moment of inertia

l_1, l_2 : Distances between the mass center and imbalance locations

l_p : Vibration pick up position

m_r : Rotor mass

M_{ξ_U}, M_{ψ_U} : Moments induced by imbalance of rotor

p_a : Ambient pressure

p_j : Pressure developed in journal bearing

P_j : Nondimensional pressure of journal bearing, $P_j = \frac{p_j}{p_a}$

r : Radial coordinate

r_{gc} : Centrifugal growth of rotor

R_{rot} : Radius of the rotor

t : Time

u_1, u_2 : Imbalance radius

Z : Non-dimensional axial coordinate, $Z = \frac{z}{R}$

\bar{R}_c : Response to calibrated imbalance

\bar{R}_b : Response to baseline imbalance

\bar{R}_t : Response to total imbalance

\bar{R} : Phasors of response

R_g : Gas constant of air

Greeks

δ : Top foil deflection

θ : Circumferential coordinate

Λ : Bearing number

μ : Viscosity of air

ν : Poisson's ratio

ρ_r : Density of rotor

φ_p : Angular location of added imbalance from reference

φ_b : Angular location of baseline imbalance from reference

φ_c : Angular location of the calibrated imbalance from reference

τ : Nondimensional time, $\tau = \omega t$

ξ, ψ : Angular displacement of rotor

ω : Rotating speed

ω_s : Excitation frequency

θ : Circumferential coordinate

α : Phase angle of response

η : excitation frequency ratio

CHAPTER 1

INTRODUCTION

For years, Microturbomachinery has demanded light weighted, compact and extreme temperature operation. One of the major hindrances in this respect was the use of oil as lubrication, which requires an external pressurizing unit which in turn makes the system much heavier and less compact. Though oil lubricated bearings have better performance at high temperature operation, they have been least preferred when cleaner operating environment is desired. Taking these factors into consideration, researchers have been trying to develop an air lubricated bearing which facilitates for a cleaner and more compact work environment. These bearings are more popularly known as air lubricated bearings.

1.1. Air Foil Bearing

Air foil bearings have found many applications in small to mid-sized turbomachinery. A significant advantage of compliant foil journal bearings compared to conventional rigid surface bearings is their superior dynamic performance in rotor systems. Nowadays, many high speed turbomachinery implement air foil bearings in order to improve their mechanical efficiency. AFB's have greater reliability (when designed and installed properly) compared to rolling element bearings as a result of reduced friction and oil free operation, consequently resulting in reduced scheduled maintenance.

For over three decades, air cycle machines for aircraft cabin pressurization use simple Air foil bearings (AFB). Air foil bearings used in Boeing 747 aircraft have demonstrated a robust service life with Mean Time Before Failure (MTBF) exceeding 100,000 hours [1]. Other applications include rotary flow compressor, micro-turbines [1] and oil-free turbochargers [1].

Description of simple foil bearing is shown in Figure 1.1. Foil bearings comprises of compliant surfaces of one or more layers of smooth top foil which forms the bearing surface and corrugated sheet metal bump foils which provides resilient support to the top foils. The compliant

surface provides bearing structural stiffness. Coulomb-type damping arises in AFBs due to the relative motion between the bumps and the top foil, and between the bumps and the bearing housing [2]. AFBs generally operate with ambient air. However, some specific applications use other fluids such as helium, xenon, liquid nitrogen and liquid oxygen [3].

1.1.1.Principle of Operation

Ideally air foil bearings (AFB) are best suited for high speed rigid rotors with large and uniform diameter, operating below their first bending critical speed. However, air foil bearings are often considered with flexible rotors with locally large shaft diameter in regions where the bearings are located. AFBs consist of a smooth top foil and an underlying corrugated type bump foils which together act as a compliant structure. Coulomb type friction exists between the top foil and bump foil and simultaneously between the bump foils and the bearing sleeve. The rotor and the bearing surface are separated by a void which is termed as the nominal radial clearance of an AFB. This clearance is necessary in order to initiate the formation of a hydrodynamic air film.

A hydrodynamic pressure is developed in this annulus due to the viscous drag of the spinning rotor. The hydrodynamic film created by rotor spinning causes the top foil and elastic structure to retract resulting in finite film thickness comparable to rigid-walled gas bearings [4], [5], thus enabling high speed operation and larger load capacity [1]. This characteristic of AFBs also facilitates for rotor misalignments, thereby increasing their reliability. The air film is created around the circumference of the bearing surface due to the pressure gradient around the circumference and shear flow. Also, when the rotor sits on the bearing surface (top foil), rotor center is automatically offset from the bearing center creating initial wedge necessary for the hydrodynamic pressure development.

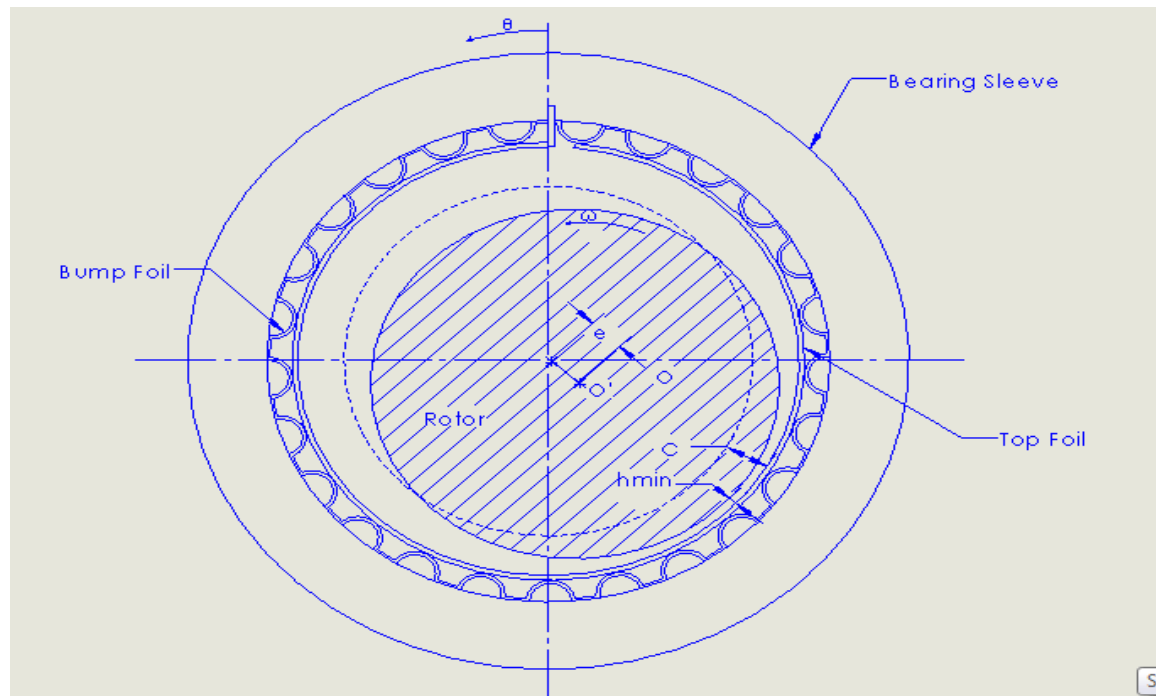


Figure 1.1 Schematic of a circular top foil, continuous bump air foil bearing showing eccentricity and radial clearance

Despite having a greater service life and reduced maintenance, AFBs have issues concerning dry rubbing during start/stop operations of the rotor. Top foil surface coated with low friction coefficient solid lubricants like Teflon have been used in order to reduce friction during this rubbing. Another drawback with AFB has been its heat dissipation capability. Parasitic heat energy developed due to viscous heating due to high speed operation is not easily dissipated. In addition, heat conducted from various parts of the machine can be too much for the air foil bearing to dissipate them effectively, resulting in thermal runaway. The hydrodynamic pressure generated between the rotor and bearing surface only provides load capacity and does not dissipate heat energy developed in the bearing. In order to overcome these issues, a hybrid air foil bearing (HAFB) has been developed recently. These bearings operate on hydrodynamic conditions in the presence of a hydrostatic lift, thereby giving them the name hybrid. These bearings have greater load capacity [3] and heat dissipation capacity.

1.1.2. Introduction to Hybrid Air Foil Bearing

Hybrid air foil bearing (HAFB) operates under hydrodynamic pressure in the presence of externally pressured hydrostatic air. Experiments on HAFBs show their enhanced heat dissipation capability and load carrying capacity [6].

Externally pressurized air is fed into the annulus between rotor and the bearing surface through orifice tubes attached to the top foil. It was shown that increase in external air supply pressure increased the critical speed of synchronous vibration [7]. Increase in external air supply pressure also tends to center the rotor thereby resulting in decrease in direct stiffness and also increase in direct damping of the rotor bearing system. It also reduced the effects of cross coupled stiffness which is a major factor causing bearing instability [8]. Another major advantage of HAFBs is the cooling effect external air has on the rotor, thereby minimizing the thermal distortions [6]. Figure 1.2 shows the HAFB configuration used in [8].

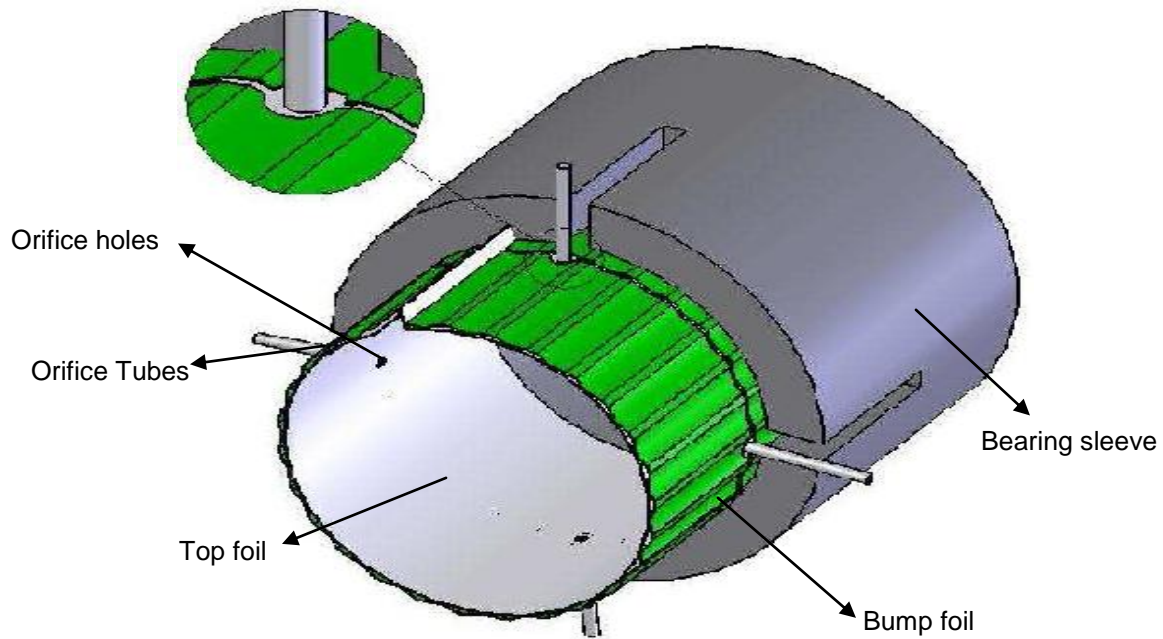


Figure 1.2 Schematic of a Circular top foil HAFB used by previous researchers

1.1.3. Configuration of Three- Pad HAFB

The bearing discussed in this article has a three pad configuration (Pad A, B and C), as shown in Figure 1.3 with each pad having an arc angle of 120° . The bearing consists of 3 top foils and 6 bump foils, with a pair of bump foils forming the compliant structure with individual top foil. Each pad has its center offset from the global center by a small distance. This type of configuration gives varying nominal clearance around the circumference of the rotor, with maximum clearance at the leading and trailing edge of the top foil and minimum clearance equal to the set bore clearance at the center of the arc length of the top foil. Figure 1.3 shows the schematic of a three pad hybrid air foil bearing showing preload and nominal clearance.

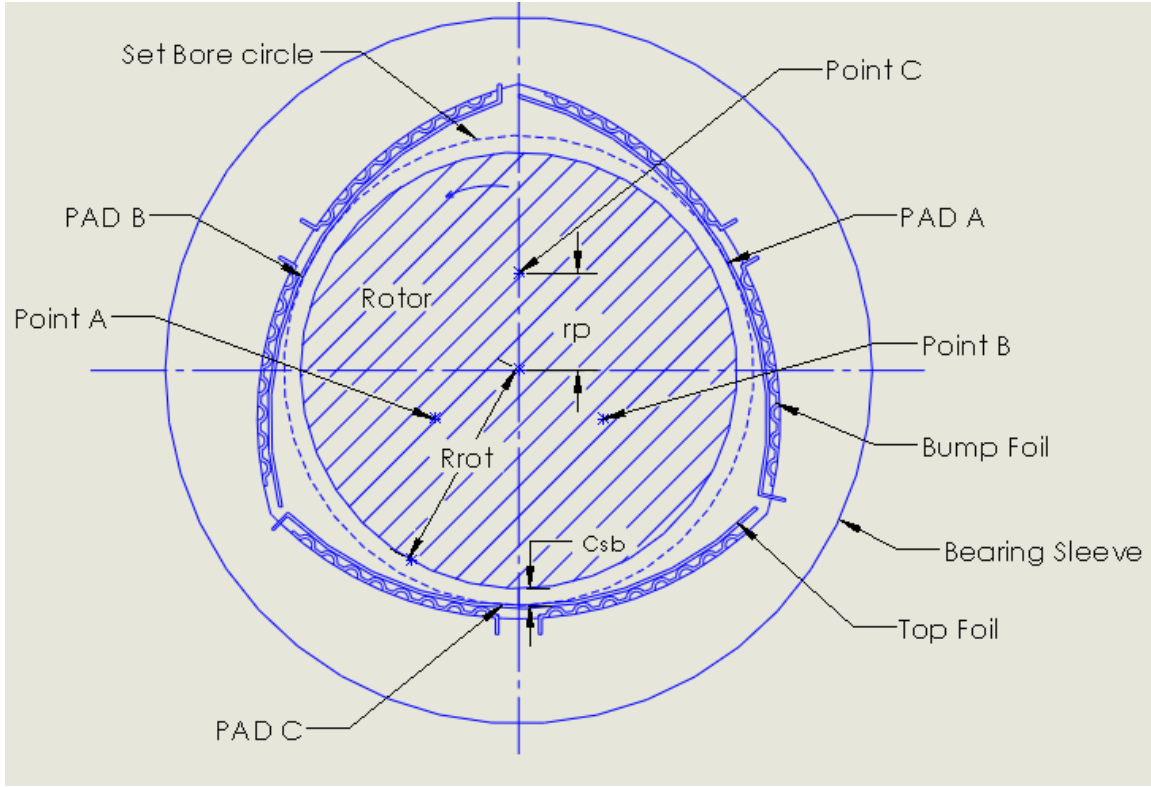


Figure 1.3 Schematic of a HAFB showing preload, set bore clearance and pad configuration

The pad A,B and C shown in Figure 1.3 have their centers at point A, B and C respectively

The numerical relation between preload and set bore clearance is as shown below

The radius of the pad is given by

$$R = r_p + R_{Rot} + C_{SB} \quad (1)$$

The nominal journal bearing clearance is given by

$$C_j = R - R_{Rot} \quad (2)$$

Substituting equation (1) in equation (2)

$$C_j = r_p + C_{SB} \quad (3)$$

The non dimensionalized bearing preload is given by

$$R_p = \frac{r_p}{C_j} \quad (4)$$

Substituting equation (3) in equation(4), we get

$$R_p = 1 - \frac{C_{SB}}{r_p + C_{SB}} \quad (5)$$

The equation (5) shows the when the set bore clearance tends to zero, the bearing pad and the rotor are touching each other, whereas when preload is equal to zero, the pad and rotor are concentric to each other.

1.2. Literature Review on Previous Experimental Study

Gas foil bearing technology has made significant progress during the last 30 years. Air Foil bearings (AFBs) fulfill most of the requirements of novel oil-free turbomachinery by increasing their reliability in comparison to rolling elements bearings. Heshmat et al [4] provides the earliest experimental and analytical studies. He provided analytical studies on bump foil stiffness, pressure profile and load carrying capacity by solving the Reynolds equation numerically.

Heshmat et al [9] presents a theoretical model of a bump type air foil bearings. He investigates the relationships between the load, deflection, stiffness, and damping of the bearing compliant elastic foundation. He also accounted for frictional forces in the modeling along with localized force interaction, bump geometry, and load distribution variation. Coulomb friction between top foil and bump foil and between bump foils and bearing sleeve was also considered in his analysis.

Peng and Carpino [5] calculated the stiffness and damping coefficient of an elastically supported Air foil bearing using a finite element model. They neglected any bending of membrane effect of the foil structure. With the film thickness given, Reynolds equation was solved using finite element methods to obtain pressure. Dynamic bearing coefficients (stiffness and damping

coefficients) of the air foil bearing were solved using perturbation method where Reynolds equation was linearized to yield force coefficients. Their results showed that the compliance of the bearing at relatively low speeds primarily depends on the hydrodynamic gas film. But, at high speeds the stiffness of the hydrodynamic gas film becomes very large and hence the compliance is due to the underlying elastic foundation.

Radil et al [10] studied the dependence of load capacity of air foil bearings on the radial clearance. They showed that air foil bearings have an optimum radial clearance, below which thermal run-away can occur in the bearing leading to gas film rupture. He also showed that at clearances beyond the optimum value, the load carrying capacity of the bearing is reduced.

A simple rule of thumb was introduced by Dellacorte and Valco [11] to estimate the load capacity of air foil bearings. Using the data available from previous literature and experiments performed by the authors, relationship between load capacity of the bearing to the bearing size and operating speed was developed.

Iordanoff [12] developed an analytical formula for evaluation of the bump foil stiffness for free end and clamped end (welded) conditions. Typical analyses of bump strips include the dry-friction forces between the top foil and bumps, the housing and bumps, and the coupling forces with adjacent bumps. Bending moments exist at the support points of the bump foil where connection is made with the bearing sleeve. However, formulas for the bump stiffness provided by the author does not consider bending moments at the bump supports and within the straight contact patch which connects the bumps.

Recently, Song and Kim [13] developed a new kind of bearing whose compliant structure is made of commercially-available compression springs. They performed analytical and experimental studies to determine the performance of this new bearing. Stiffness of the springs under lateral loading was calculated analytically and then validated with experimental investigation. Load capacity, equivalent viscous damping and structural loss factor were also measured to demonstrate the feasibility of the new bearing. Analytical studies also included a time-domain orbit simulations that could predict limit cycle behaviors encountered in air foil

bearings. The results showed that the damping of underlying structure can suppress the maximum peak at the critical speed very effectively but not the onset of hydrodynamic rotor-bearing instability. Experiment results also showed that the bearing could have large load capacity in the presence of appropriate cooling. This observation is believed to be true with any air foil bearings with different types of compliant elastic foundations.

Furthermore, Kim [14] conducted parametric studies on two different types of air foil bearing configurations, one with circular bearing surface and other having a three-pad configuration. He investigated the dependence of rotor dynamic stability on the distribution of stiffness and damping of the compliant surface. The study showed that rotordynamic stability is more dependent on bearing geometry rather than the stiffness and damping of the elastic foundation. The author performed linear stability analysis and orbit simulations and found different onset speed of instability from the two methods. The discrepancy in results between the two methods was attributed to the limitation of linear stability analysis in the stability predictions. The force coefficients used in the linear stability analyses are calculated from the linearized Reynolds equation. However the force coefficients depend on the excitation frequencies and rotor running speeds rendering the equations of rotor motion highly nonlinear. This assumption affects the accuracy of linear stability analysis. Also, rotor imbalance response can be much higher than the perturbed motion which is taken into account while solving the linearized Reynolds equation, from which the force coefficients are determined. This is another limitation of linear stability analysis

One of the major issues with air foil bearings is its heat dissipation capability. At high speed operation of the rotor bearing system, viscous heating takes place which results in development of parasitic heat energy at the bearing locations. In addition to this, the heat is conducted from various parts of the machine to the bearing location. This heat is not easily dissipated eventually resulting in thermal runaway of the bearing. In order to overcome these problems, researchers have tried to develop a hybrid air foil bearing (HAFB), which operates in the presence of hydrostatic lift up air.

Kim and Park [15] developed air foil bearing with external air pressurization. Compression springs arranged axially formed the compliant structure and was similar to the bearing used in [13]. This bearing is a hybrid bearing as it operates on both hydrodynamic and hydrostatic conditions. Four external orifice tubes were used for external pressurization, which was done through the bump foil and top foils. The numerical investigation was performed to determine the pressure profile and film thickness of the bearing under hybrid operation and compared with results from hydrodynamic condition. Coast-down simulations for the bearing were also performed. The simulation results showed that hybrid operation increased the onset speed of bearing instability as compared to hydrodynamic operation. They also showed that load capacity of the bearing under hybrid operation was higher compared to hydrodynamic operation. Hybrid operation also showed reduced friction torque during start up / shut down of the rotor.

Recently, Kim and Manish [3] conducted parametric study on the dynamic performance of the HAFB. They performed both analytical (linear perturbation analysis developed for HAFB's) investigation on a HAFB to determine its stiffness and damping coefficients. Results showed that feed parameter and supply pressure affects the dynamic characteristics of HAFB. With an increase in either the supply pressure or the feed parameter, the rotor centers itself and thus the direct stiffness decreases. Direct damping showed increasing trend with the supply pressure and the feed parameter, thereby reducing the instability forces within the bearing. They also showed that the cross-coupled stiffness, which is the primary cause for bearing instability, could be reduced by increasing either the supply pressure or the feed parameter.

1.3. Objective of Current Research

In this article a four degree of freedom rigid rotor supported by two three-pad HAFB and an air lubricated thrust bearing is used to determine the imbalance response of the rigid rotor. Generally, imbalance response of a rotor has been performed considering two degrees of freedom motion. Two degree of freedom vibration analyses takes into account only cylindrical mode of vibration and makes the design analysis simple taking into account only the critical

speeds due to cylindrical vibrations. However, conical vibration mode plays a major role in imbalance response analyses as this mode of vibration is dominant during bearing failure. Conical vibrations also tend to initiate excessive loading on the bearing edge, which is difficult to predict on two degree of freedom rotor bearing model. Thus, the current two degree of freedom model cannot predict the instability and failure mode of the rotor bearing system

This paper presents the non linear imbalance response of a four degree of freedom (DOF) rigid rotor supported by two three pad air foil bearings. The translational and gyroscopic motion of the rotor has been determined by solving four non linear degrees of motion. Different vibration modes are initiated by locating imbalance masses at circumferential holes provided on the rotor edge. The effect of supply pressures on dynamic behavior of rotor bearing system is also investigated by analytical simulation.

In addition to analytical studies, imbalance response of a rigid rotor supported by both hybrid and hydrodynamic foil bearings were measured using a custom made test rig for different vibration modes and their results are compared with analytical studies. Also, the effect of varying supply pressure on imbalance response of the rotor bearing system is investigated.

1.4. Summary of Major Contributions

Imbalance Response of a hybrid three pad air foil bearing:

The test bearing has a three pad configuration compared to the circular top foil configuration adopted by previous researchers. Imbalance response of a three pad hybrid air foil bearing has never been performed till date and the test that will be performed will be the first of its kind on three pads HAFB.

Consideration of four degree of freedom rigid rotor supported by HAFB:

Previously, researchers have provided various design methods for AFB's and performed design analyses considering two degree of freedom of rotor vibration. Two degree of freedom vibration analyses takes into account only cylindrical mode of vibration and makes the design analysis simple taking into account only the critical speeds due to cylindrical vibrations. This

analysis involves effects of both translational and gyroscopic motion of the rotor, thereby enabling a better analysis of rotor bearing system, especially during critical speed and conical mode of the bearing.

CHAPTER 2

DESCRIPTION OF TEST BEARING AND TEST RIG

Previous researchers [14] performed parametric studies on a three pad air foil bearing and showed that the dynamic performance of the bearing depended on the bearing geometry rather than the force coefficients of the bearing elastic foundation. This research article deals with empirical testing of a hybrid three pad air foil using a custom made test rig to determine the imbalance response of a rigid rotor supported by two HAFB along with analytical simulations. This chapter discusses in detail the design parameters and methodology used in manufacturing of the HAFB and the test rig.

2.1. Design Parameters of Bearing

The bearing used in this research is a three pad hybrid air foil bearing. Figure 2.1 shows the schematic of a three pad HAFB with orifice tubes attached. The bearing has three top foils and 6 bump foils as shown in the figure. Externally pressurized air is supplied to the bearing through three (3) orifice tubes attached at the backside of the top foil. The orifice tubes are located at three angular locations of 60° , 180° and 300° . The three pad configuration renders different nominal radial clearances to the bearing, with maximum clearance at the leading and trailing edge of the top foil and minimum clearance at the orifice location of the top foil. Each pad of the bearing has its center offset from the global center by 0.035mm, which provides the bearing its necessary preload. The nominal radial clearance desired with the HAFB used in this article is $70\mu\text{m}$. Table 2.1 shows the parameters of the bearing used in simulations.

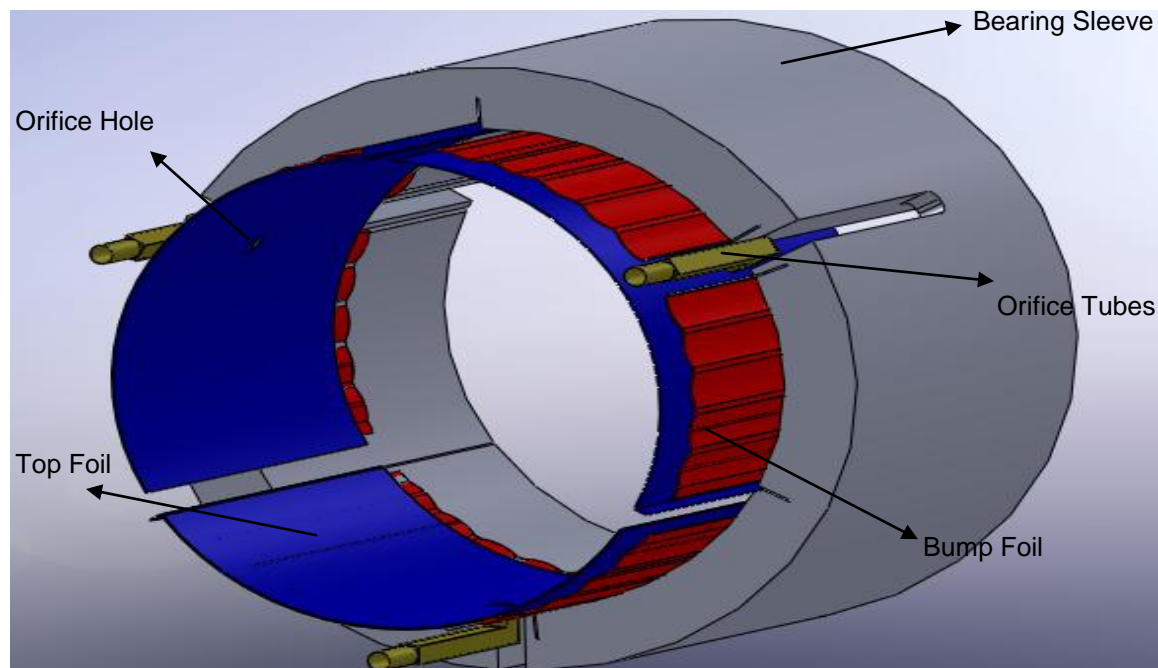


Figure 2.1 Schematic of a three pad HAFB showing top foil and bump foils

Three slots are provided on the bearing housing to accommodate the top foils as shown in Figure 2.7. Each slot is separated by an angle of 120° . Each pad on the housing is provided with 2 smaller slots to hold the bump foils. The housing also has three wide slots separated by 120° , to house the steel orifice tubes. L shaped orifice tubes (will be explained later) are brazed at the center of axial length of the top foil. The orifice tubes are designed so as to just protrude out of the bearing edge and it is then connected to plastic tubes. Split type bump foils with slots cut along its axial length is used.

Table 2.1 Bearing Parameters used in simulation

Parameter	Value
Bearing Radius R	24.5 mm
Bearing Axial Length L	37.5 mm
Bearing preload r_p	35 μm
Average Bump Stiffness	2.39E+6 N/m
Nominal radial Clearance	70 μm
Top foil thickness	0.1524 mm
Bump Foil thickness	0.127 mm
Bump Height	0.44 mm
Orifice Size (Diameter)	1 mm

2.2. Manufacturing Process of HAFB

A hybrid air foil bearing consists of four parts, namely

- Bearing Sleeve
- Corrugated bump foil
- A smooth top foil
- Orifice tubes attached to the top foil

Bearing Sleeve:

The Bearing sleeve is made up of Stainless Steel 316. The bearing sleeve consists of very intricate and narrow slots which would be really challenging to fabricate using conventional methods of machining. Thus it is machined using wire electro discharge machining (EDM), which ensures high precision within the required tolerance levels. After fabrication of the bearing sleeve it is subjected to a heat treatment condition to provide it the required strength. The heat treatment

process of SS 316 components starts with heating up at 650° C, followed by hold at 650° C for 1 hr and air cool. The process is described in Figure 2.3 .

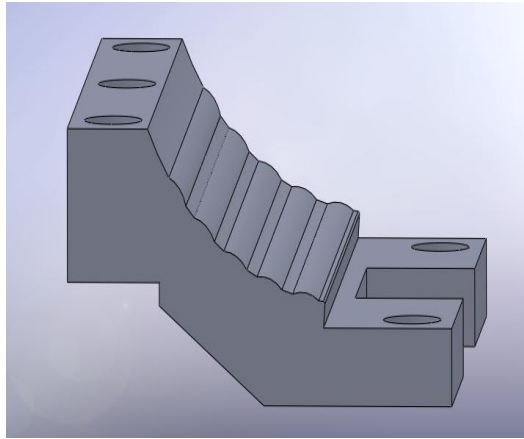
Figure 2.7 shows a schematic of the bearing sleeve with slots to accommodate bump foils, top foils and orifice tubes.

Corrugated bump foil:

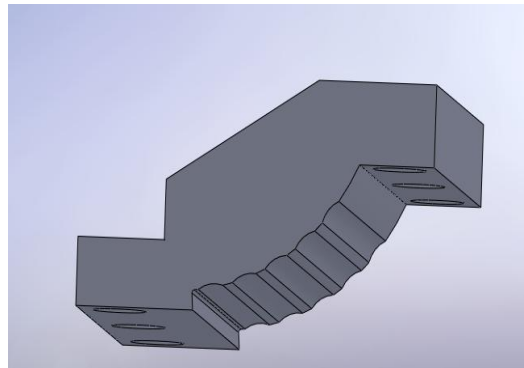
Bump foil are made up of stainless steel 316 shims of thickness 0.127 mm. These bump foils are formed by using a forming jig having a mating profile same as that of the bump foil. The upper part, lower part and assembled bump foil forming jig are shown in Figure 2.2. The forming is machined using wire EDM process.

The shim of required thickness is cut into width of 35.5 mm. It is then placed in between the two parts of the forming jig and is held in place by a forming jig holder. The two forming jig parts are pressed down with the shim placed in between them until a uniform profile is formed throughout the shim. The two parts of the forming jig are then bolted down and heat treated in a furnace in order to provide the bump foils required strength and stiffness. The heat treatment condition for stainless steel 316 is as shown in Figure 2.3.

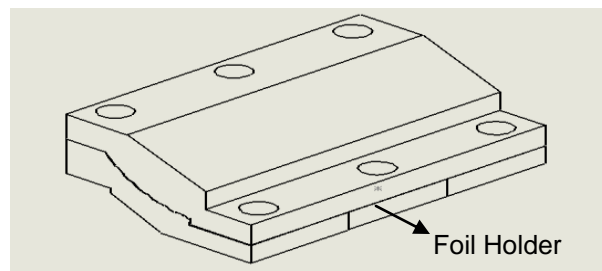
After heat treating the bump foils, slots are cut at locations as shown in Figure 2.4 using wire EDM process.



(a)



(b)



(c)

Figure 2.2 Bump foil forming jig (a) Lower Part of the jig (b) Top part of the jig (c) Isometric view of the assembled forming jig showing foil holder

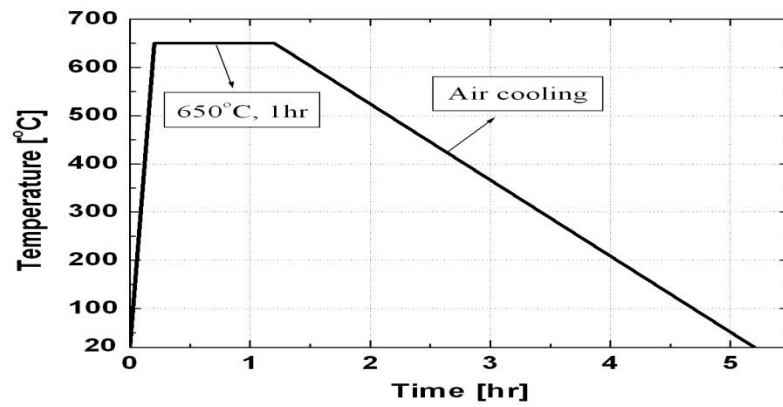
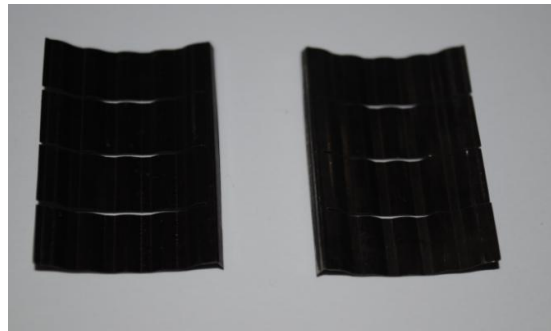
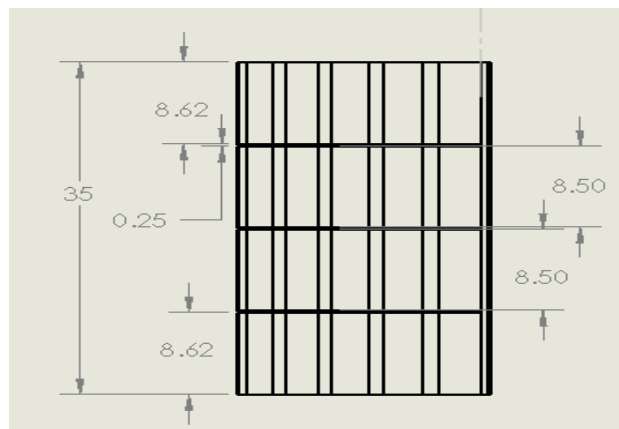


Figure 2.3 Heat Treatment for stainless steel 316



(a)



(b)

Figure 2.4 Corrugated Bump Foil (a) Bump foil with slots (b) Schematic of the bump foil showing slots

Top foil:

Top foil is made of Stainless Steel 316. Top foils are also formed using a forming jig made up of Inconel 718. A shim of 37.5 X 51.85X 0.1524 mm is placed between the two jig parts and is pressed down until the desired shape is obtained. The shim is held in place by a holder which is bolted down to the lower part of the jig. The length of the lip is controlled by means of shims laser welded to the lower part of the jig as shown in Figure 2.5. Figure 2.6 shows the assembled top foil forming jig.

Once formed, top foil is heat treated the same way as the bump foil. After heat treatment, orifice hole of 1 mm diameter is then drilled through the top foil. Orifice tubes are then soldered onto the back side of the top foil. The solder used was Silflo 430 solder for similar metal soldering along with Duzall 430 flux. Figure 2.9 shows the top foil with L-shaped orifice tubes attached.

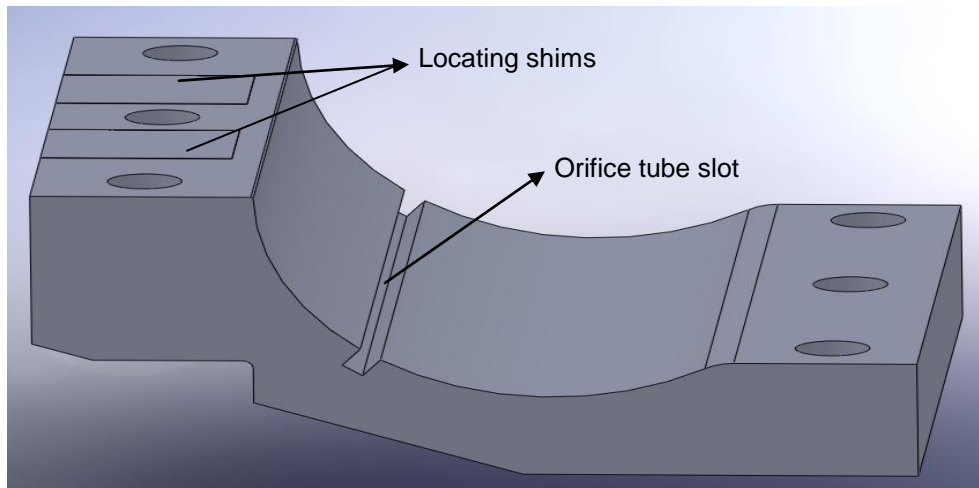
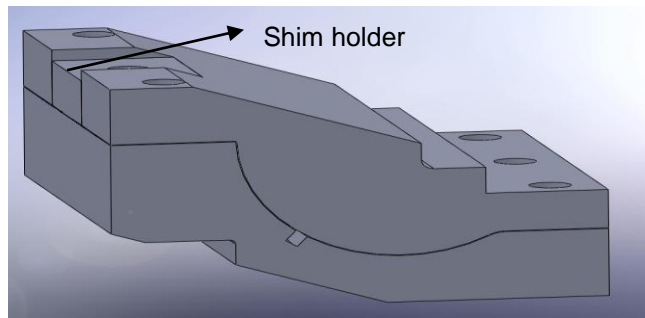
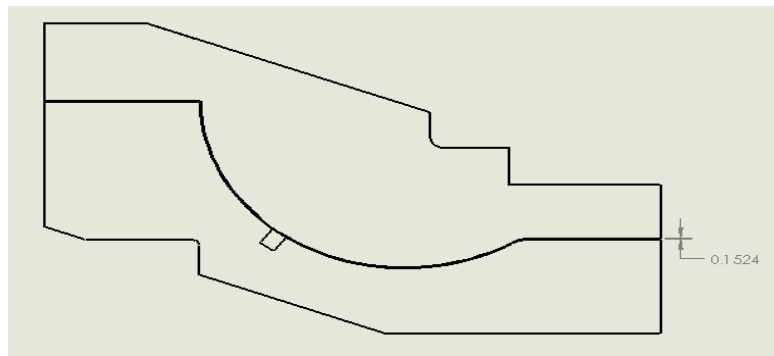


Figure 2.5 Lower part of the top foil forming jig showing orifice tube slot and locating shims

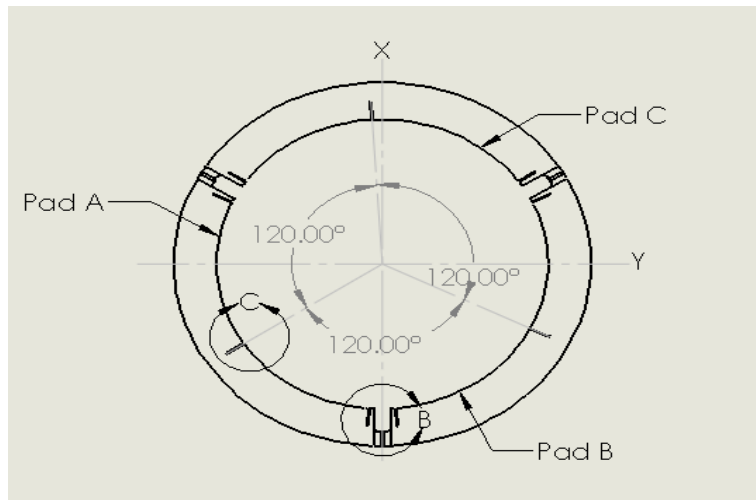


(a)

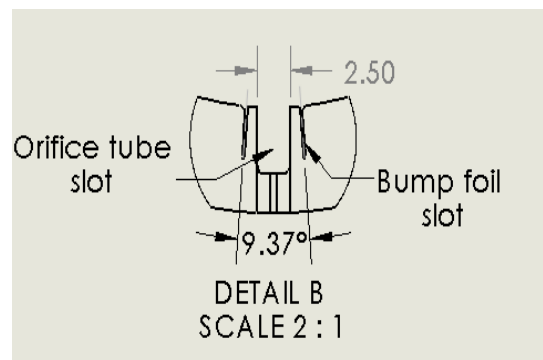


(b)

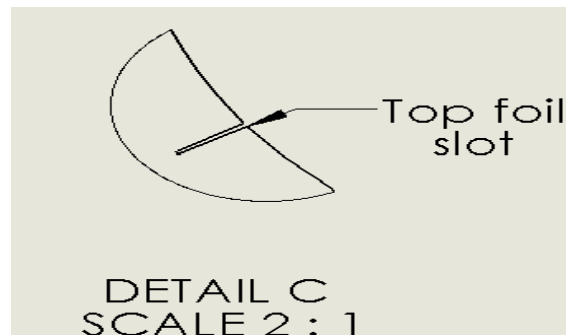
Figure 2.6 Assembled top foil forming jig (a) Assembly showing top foil holder (b) Schematic of a top foil forming jig showing annulus where top foil is formed



(a)



(b)



(c)

Figure 2.7 Schematic of a bearing sleeve (a) Bearing sleeve showing three pad configuration (b) Detailed view of the bump foil slots and the orifice tube slot on the bearing sleeve (c) Detailed view of the top foil slot

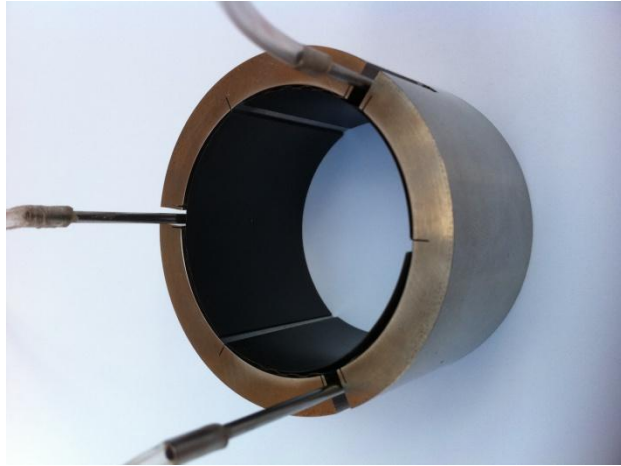
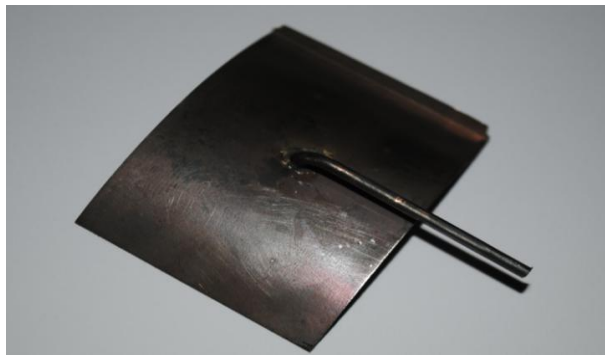
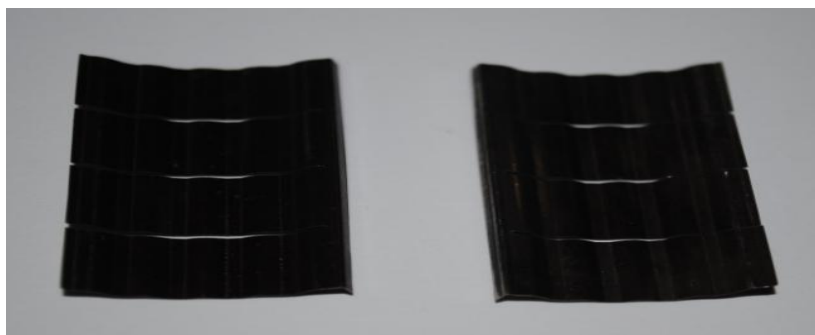


Figure 2.8 Assembled HAFB



(a)



(b)

Figure 2.9 Photo of manufactured three-pad foil bearing (a) Top foil with orifice tube attached (b) Bump foils

Orifice Tubes:

Orifice tubes are made up of stainless steel 316 of dimension 0.083 in OD, 0.067 in ID tubes. They are formed into L shape by using a forming jig made up of stainless steel 316. Figure 2.10 shows the L shaped rectangular cross section orifice tube

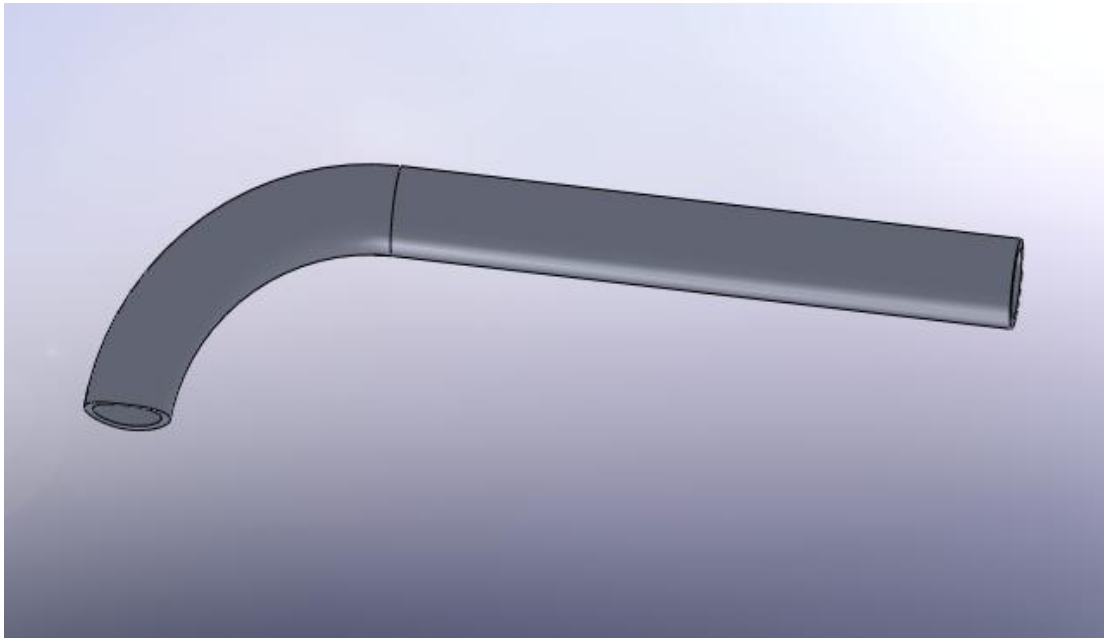


Figure 2.10 L Shaped circular cross section orifice tubes

2.3. Description of Test Rig

The design and fabrication of a test rig which could evaluate the performance of Flexure pivot tilting pad gas bearing was undertaken by previous researchers. The same test facility was used to perform imbalance response tests on a rigid rotor supported by HAFB. This section describes this unique test rig and its capabilities.

The main requirement of this test rig is to measure the imbalance response of a rotor supported by HAFB at different imbalance orientation of 0° , 90° and 180° . The other purpose of this test rig is to determine the role of external supply pressure on the imbalance response of the system.

Figure 2.11 shows the general layout of the test rig housing two hybrid air foil bearings.

Description of the individual components shown in the figure is given below:

1. Electric motor: The motor is a 2-pole, asynchronous, high-speed and medium frequency motor, with maximum speed of 50000 RPM
2. Motor stator: Stator for the electric motor.
3. Cooling jacket: Cooling jacket is provided in order to dissipate heat during high speed operation of the motor, thereby enhancing its performance. Figure 2.13 and Figure 2.14 shows the cooling jacket used along with the stator. The cooling medium is air and its flow channel is as shown in the figure.
4. Hybrid air foil bearings: Two HAFB are used as shown in the Figure 2.1
5. Bearing inserts: Split type bearing inserts are used whose outer diameter is same as the bearing location of the test block.
6. Test section: Section of the rotor over which the HAFB is mounted
7. Rotor: Spinning rotor of diameter 49 mm, 359 mm long, having imbalance mass slots at its ends. Cross sectional view of the rotor is shown in Figure 2.16
8. Thrust Pads: The rotor is supported by a thrust bearing to minimize axial loading of the rotor. The thrust bearing comprises of two thrust pads and a thrust spacer. Air injection orifices are provided on the thrust pad. Figure 2.17 shown the complete assembly of the thrust pads and the thrust spacer.
9. Thrust spacer: Thrust spacer is used in order to provide enough space for a constant air film to develop between the rotor disc and the individual thrust pads.
10. Test Block: The entire test rig is housed inside a test block. The test block comprises of a lower part and an upper part and is made up a stainless steel to make the rig rigid and robust.
11. Base plate: The entire test block is mounted on a base plate made of stainless steel.

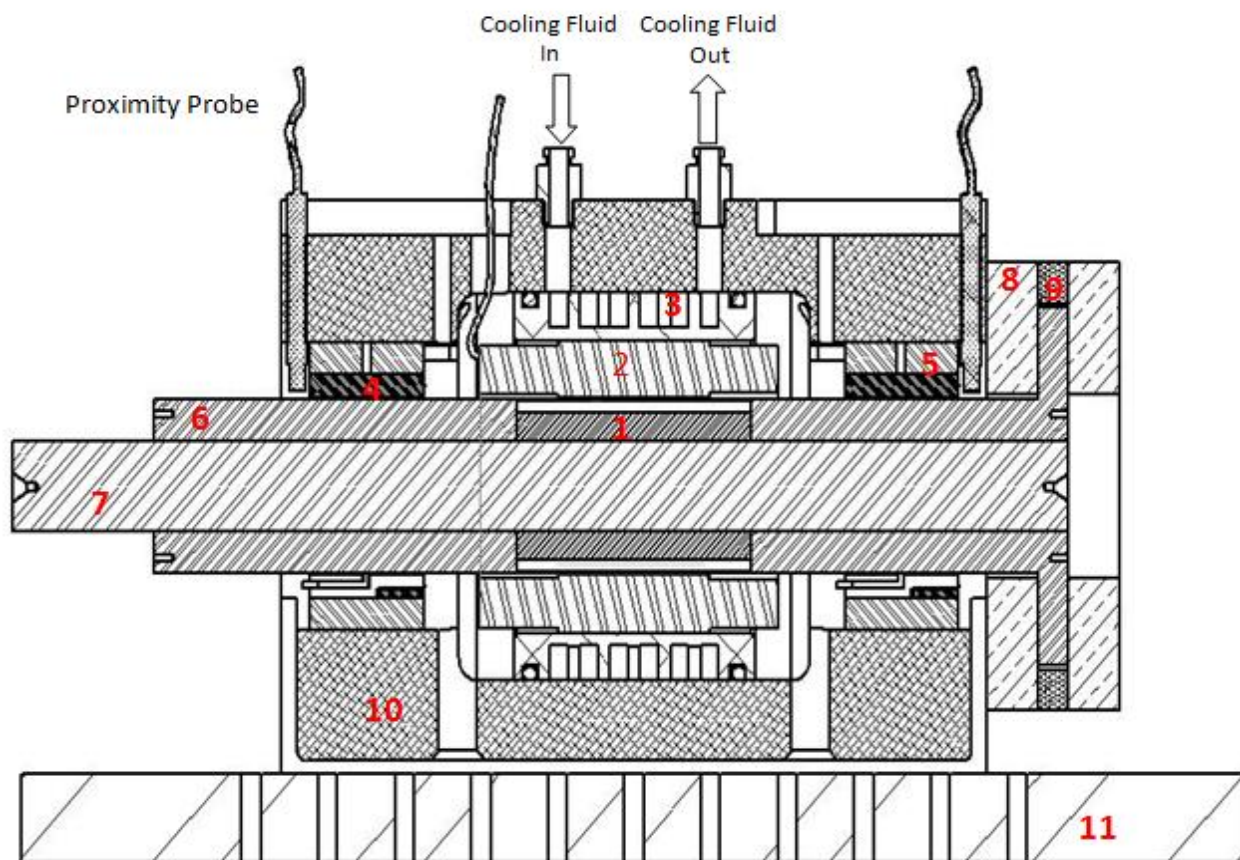


Figure 2.11 General Layout of the test rig

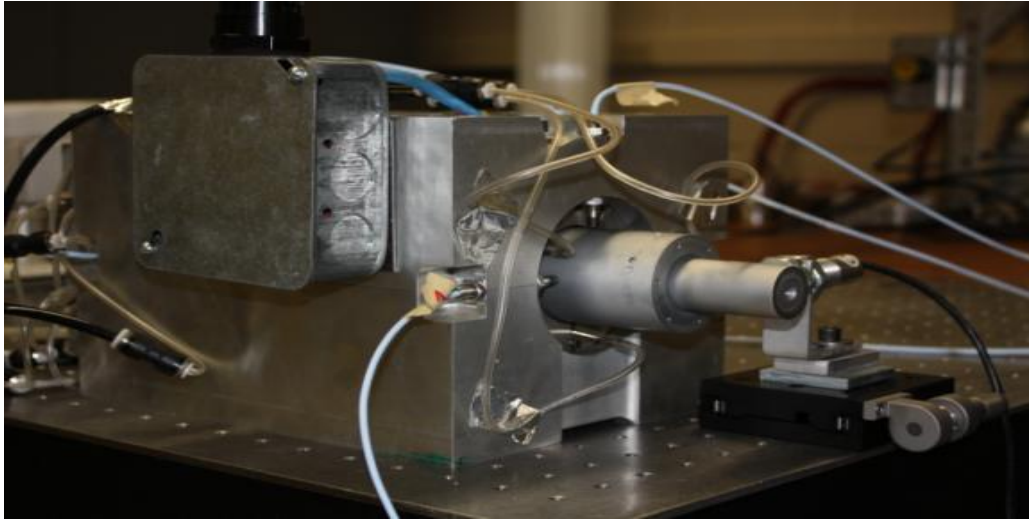
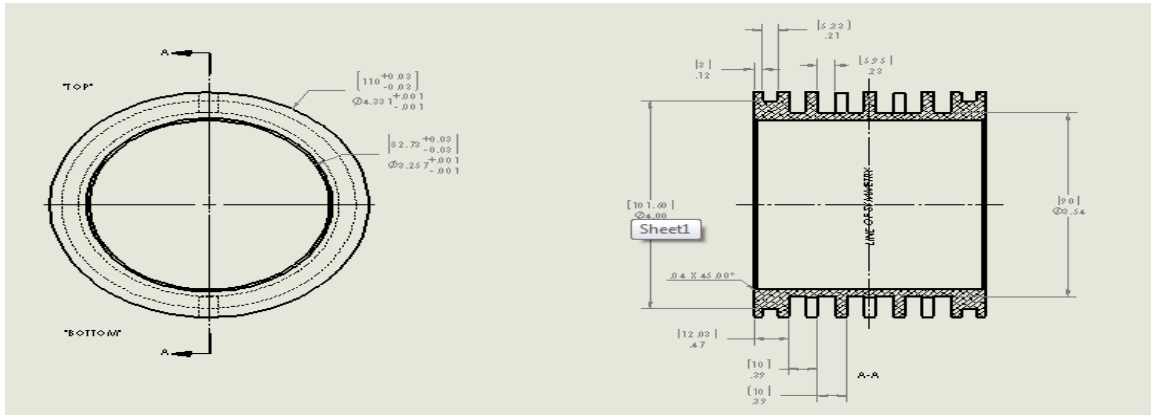


Figure 2.12 Picture of the test facility

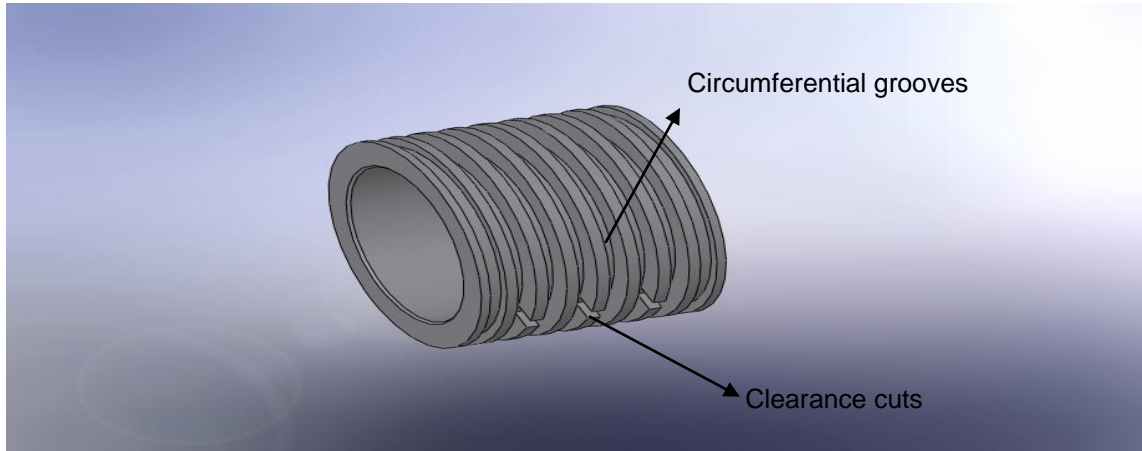
Detailed description of major components of the test rig is as mentioned below,

Electric Motor:

The motor is a 2-pole, asynchronous, high-speed and medium frequency motor. The motor has a wound stator and a raw rotor. Air is used as coolant for the cooling jacket. The cooling jacket has circumferential grooves which act as channels for the flow of cooling air as shown in Figure 2.13. Clearance cuts are provided on the cooling jacket which facilitates the flow of cooling air from one circumferential groove to another. Figure 2.14 shows the assembly of the motor stator and its cooling jacket

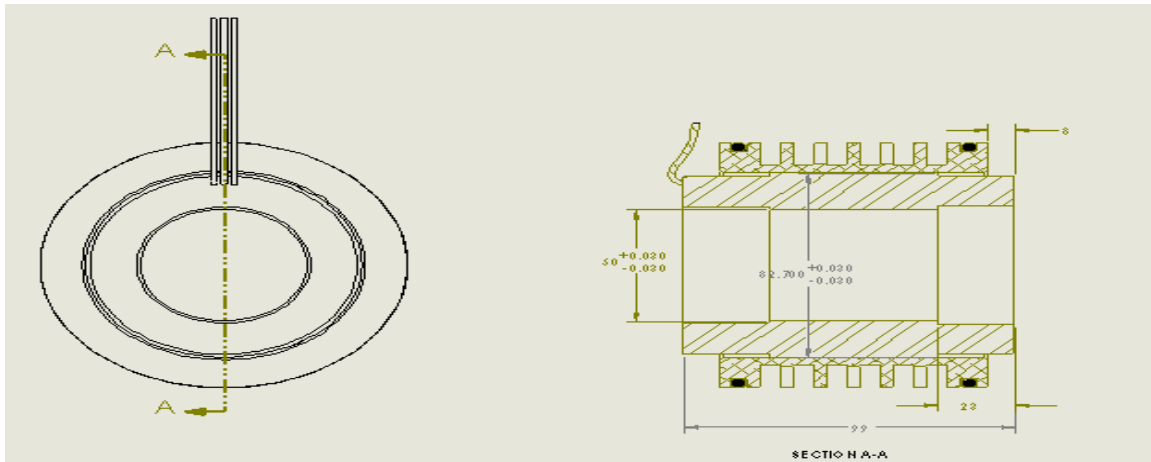


(a)

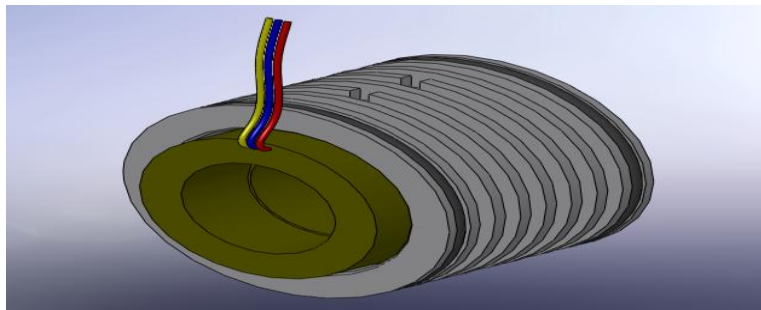


(b)

Figure 2.13 Motor cooling jacket (a) Schematic of the cooling jacket and its cross section (b) Cooling jacket showing circumferential grooves and clearance cuts



(a)



(b)

Figure 2.14 Assembly of the stator and cooling jacket (a) Schematic b) Assembled stator and cooling jacket

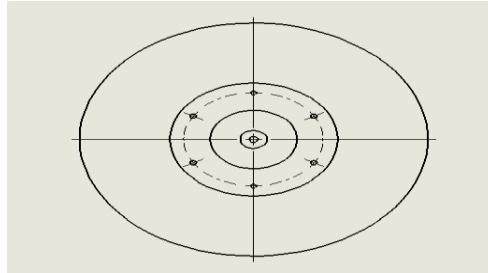
Rotor:

The rotor comprises of three parts namely,

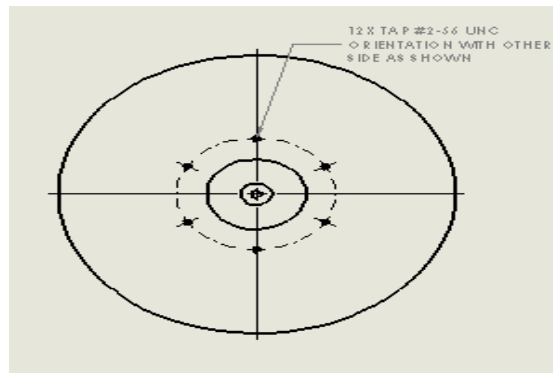
- Center shaft
- Test inserts
- Thrust disc

Center shaft, test inserts and the thrust disc is made up of stainless steel. The rotor is also provided with small grooves of #2-56 UNC tap at both its ends so as to accommodate the imbalance masses as shown in Figure 2.15. The grooves are located at six locations on each side with each groove circumferentially offset by 45°. An interference fit exists between the center shaft and the test inserts. The motor element is mounted at the center of the shaft. Figure 2.16

shows the schematic of the rotor and the cross sectional view of the rotor assembly showing test inserts, thrust disc and imbalance mass grooves. Table 2.2 shows the specifications of the rotor

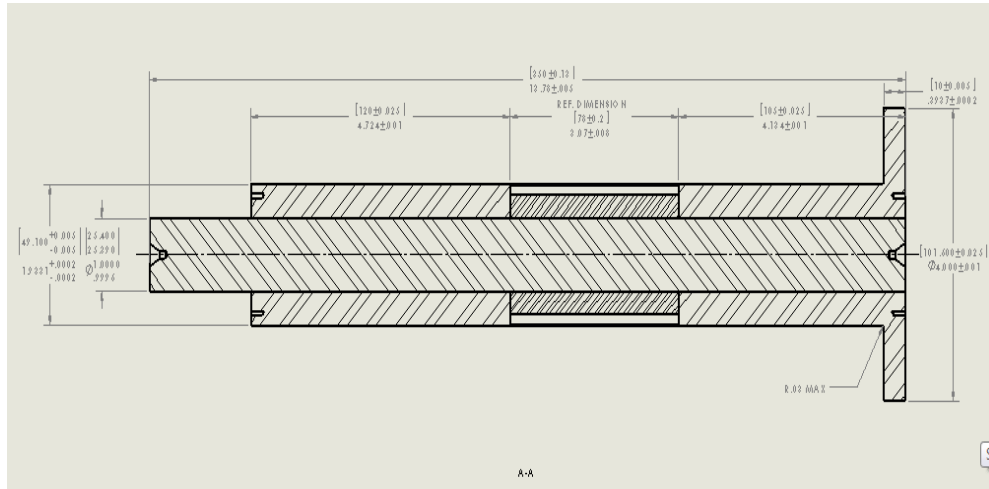


(a)

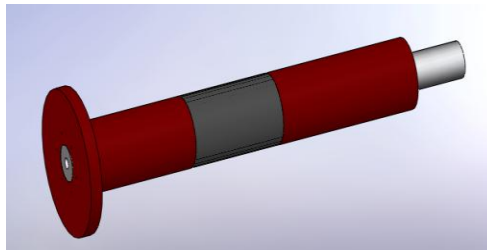


(b)

Figure 2.15 Mass imbalance grooves on the rotor (a) front view (b) rear view



(a)



(b)

Figure 2.16 Rotor (a) Cross section of the rotor showing test section, motor element and thrust disc (b) Schematic of the rotor assembly

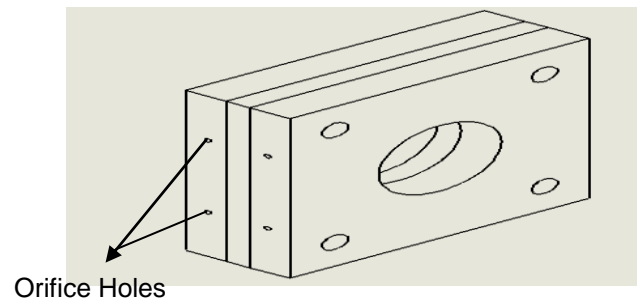
Table 2.2 Specifications of the rotor used for simulation

Parameter	Value
Radius	24.5 mm
Length (l_r)	286 mm
Mass (m_r)	4.8678 Kg
Translational moment of inertia (I_T)	0.0509 kgm ²
Polar moment of inertia (I_p)	2.0224X 10 ⁻³ kgm ²

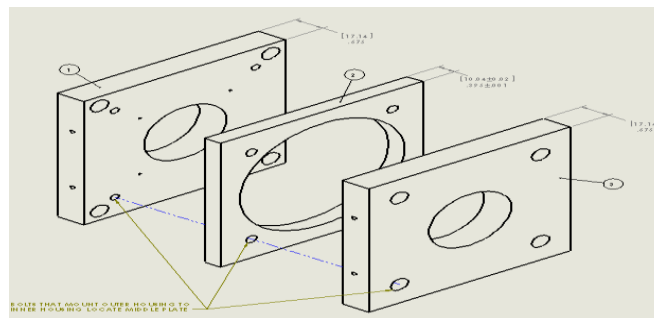
Thrust Bearing:

The axial motion of the rotor during high speed operations is cushioned and minimized by using a thrust bearing. The thrust bearing is air lubricated and it comprises of two thrust pads and a thrust spacer. The purpose of the spacer is to provide room for generation of uniform air film between the pads and the spacer. The spacer thickness is 0.040 mm greater than the thickness of the thrust disc, thereby enabling an air film of 0.020 mm thickness between each thrust pad and the thrust disc. The cushioning air is supplied externally by means Teflon tubes through the orifice holes provided on the side face of both thrust pads.

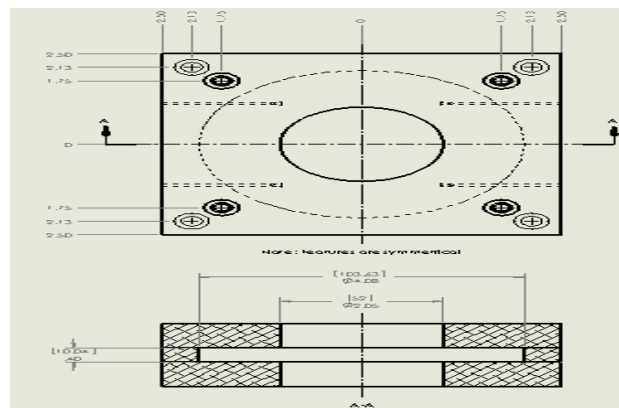
Though the thrust bearing minimizes axial loading of the rotor, translation motion of the rotor is not completely diminished. However, for simplicity of design and analysis, axial motion of the rotor is not considered in the current research analysis. Figure 2.17 shows the assembly of the thrust bearing along with the spacer and the thrust pads.



(a)



(b)



(c)

Figure 2.17 Thrust Bearing Assembly (a) Assembled thrust bearing showing orifice holes (b) Exploded view of the thrust bearing showing outer pad inner pad and thrust spacer (c) Cross sectional view of the thrust bearing assembly

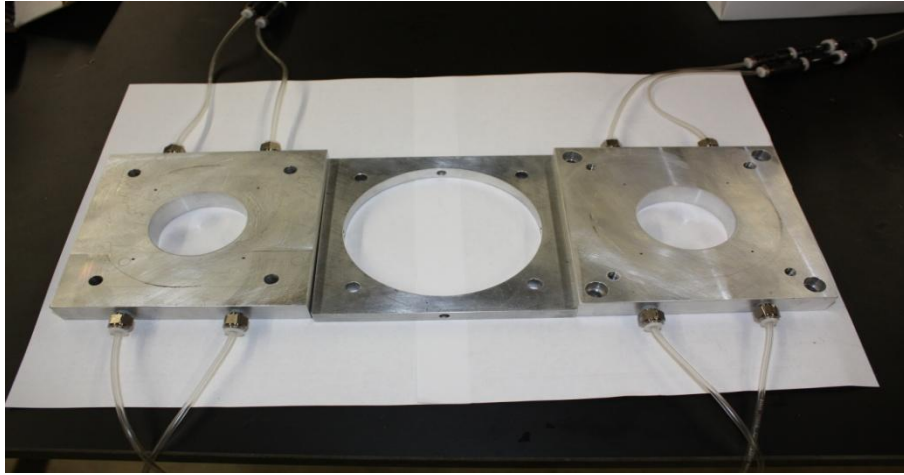


Figure 2.18 Thrust bearing components

CHAPTER 3

METHODOLOGY

This section elaborates the solution methodology adopted in analysis of imbalance response of a four degree of freedom rotor supported by two hybrid air foil bearings and a air lubricated thrust bearing.

In the model presented in this paper, the rotor has both translational and angular gyroscopic motions and these motions are determined by solving four DOF nonlinear equations of rotor motions. The dynamic gas bearing reaction forces and moments are determined by solving the transient Reynolds equations applied to all the HAFBs. Using the developed model, various characteristic behavior of rotor supported by HAFBs was evaluated. They include 1) imbalance responses of rotor under hydrostatic operating mode for various imbalance locations 2) imbalance response of rotor under hydrodynamic operating mode for various imbalance locations 3) Effect of external hydrostatic air pressure on imbalance response of the rotor,

3.1. Theory and Governing Equations

The rotor bearing model considered in this paper is as shown in Figure 3.1. A thrust disc is located at the rear end of the rotor which is housed by a thrust bearing so as to support the thrust load of the rotor. The gravitational loading of rotor is supported by two HAFBs. The configuration of a HAFB is as shown in Figure 1.3 and Figure 2.1. Figure 3.2 shows the coordinate system used and different variables denoting rotor motion.

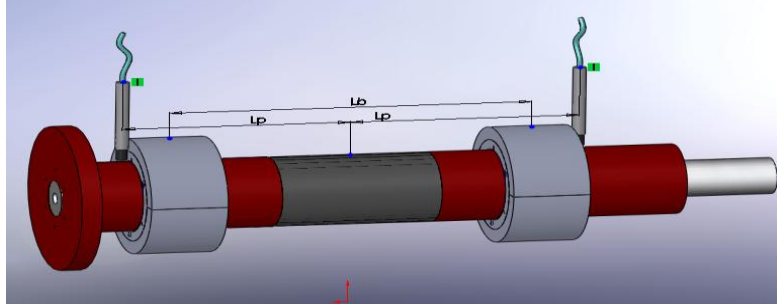


Figure 3.1 Rotor bearing system

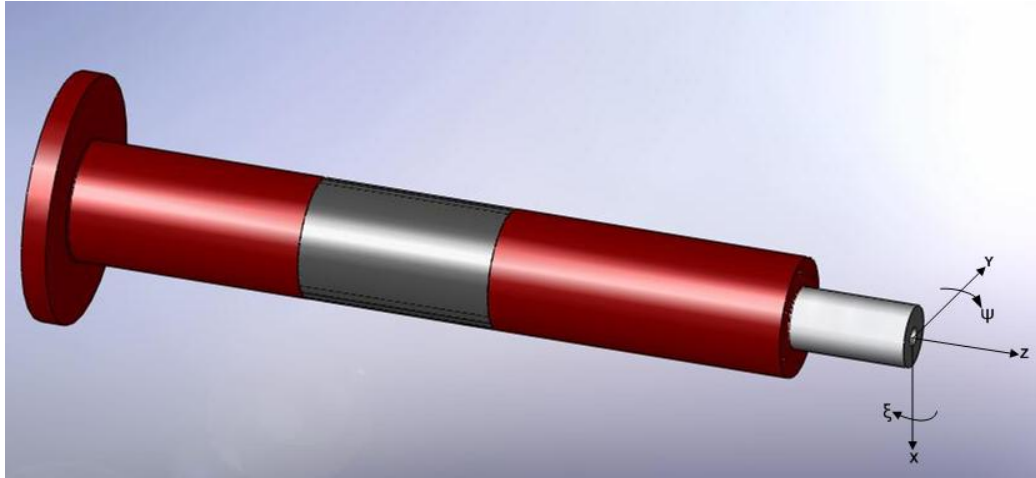


Figure 3.2 Rotor showing co ordinate system used for analysis

In the analysis, four DOF rotor motions (two translational motions e_x and e_y , along X and Y direction respectively and two rotational motions ξ and ψ about X and Y direction respectively, are considered. The rotor motions are determined by solving following governing equations.

The equations of motion for radial motions are given by equation(6),

$$\begin{aligned} m_r \ddot{e}_x &= m_r g + F_{x_B} + F_{x_U} \\ m_r \ddot{e}_y &= F_{y_B} + F_{y_U} \end{aligned} \quad (6)$$

Equations of motion for conical motion is equation (7)

$$\begin{aligned} I_T \ddot{\xi} + I_P \omega \dot{\psi} &= M_{\xi-B} + M_{\xi-U} \\ I_T \ddot{\psi} - I_P \omega \dot{\xi} &= M_{\psi-B} + M_{\psi-U} \end{aligned} \quad (7)$$

In the equations(6) and (7) , I_T is a translational moment of inertia of the rotor, and I_P is a polar moment of inertia of the rotor. F_{X-U} , F_{Y-U} , $M_{\xi-U}$ and $M_{\psi-U}$, are forces and moments induced by imbalance mass of the rotor. F_{X-B} , F_{Y-B} , $M_{\xi-B}$ and $M_{\psi-B}$ are forces and moments induced by journal bearings.

Those forces and moments due to mass imbalance of the rotor are given by the equation(8) and equation(9);

$$\begin{Bmatrix} F_{X-U} \\ F_{Y-U} \end{Bmatrix} = \begin{Bmatrix} m_r u_1 \cos \omega t + m_r u_2 \cos(\omega t + \phi_p) \\ m_r u_1 \sin \omega t + m_r u_2 \sin(\omega t + \phi_p) \end{Bmatrix} \quad (8)$$

where u_1 and u_2 are imbalance radii from the global center of the rotor, and ϕ_p is an angle between imbalances at both planes 1 and 2

$$\begin{Bmatrix} M_{\xi-U} \\ M_{\psi-U} \end{Bmatrix} = \begin{Bmatrix} m_r u_1 \sin \omega t \cdot l_1 - m_r u_2 \sin(\omega t + \phi_p) \cdot l_2 \\ -m_r u_1 \cos \omega t \cdot l_1 + m_r u_2 \cos(\omega t + \phi_p) \cdot l_2 \end{Bmatrix} \quad (9)$$

Where l_1 and l_2 is axial distance between the mass center of the rotor and imbalance mass locations.

The Bearing reaction forces and moments are given by the equations (10) and (11)

$$\begin{Bmatrix} F_{X-B} \\ F_{Y-B} \end{Bmatrix} = \begin{Bmatrix} \iint p_{j_left} \cos \theta r d\theta dz + \iint p_{j_right} \cos \theta r d\theta dz \\ \iint p_{j_left} \sin \theta r d\theta dz + \iint p_{j_right} \sin \theta r d\theta dz \end{Bmatrix} \quad (10)$$

Where p_{j_left} and p_{j_right} are the pressures developed in the left and right journal bearing respectively.

$$\begin{Bmatrix} M_{\xi-B} \\ M_{\psi-B} \end{Bmatrix} = \begin{Bmatrix} -\iint z p_{j_left} \cos \theta r d\theta dz - \iint z p_{j_right} \cos \theta r d\theta dz \\ \iint z p_{j_left} \sin \theta r d\theta dz + \iint z p_{j_right} \sin \theta r d\theta dz \end{Bmatrix} \quad (11)$$

The bearing reaction forces and moments are calculated by solving time-dependent Reynolds equations for journal. Reynolds equation for journal bearing is given by

$$\frac{\partial}{\partial x} \left(-\frac{1}{12\mu} \frac{p_j}{R_g T} h_j^3 \frac{\partial p_j}{\partial x} + \frac{R\omega}{2} p_j h_j \right) + \frac{\partial}{\partial z} \left(-\frac{1}{12\mu} p_j h_j^3 \frac{\partial p_j}{\partial z} \right) + \frac{\partial(p_j h_j)}{\partial t} = \frac{R_g T \dot{m}_s}{\Delta x \Delta z} \quad (12)$$

\dot{m}_s is the non dimensionalized mass flow rate through the orifice.

The derivation procedure of the Reynolds equation used in this thesis is as follows.

When dynamic mass balance is applied to the control volume surrounded by dotted lines in Figure 3.3. The solution methodology followed in this paper is based on Finite Volume methods. Grid scheme used for control volume and dynamic mass balance is shown in Figure 3.3.

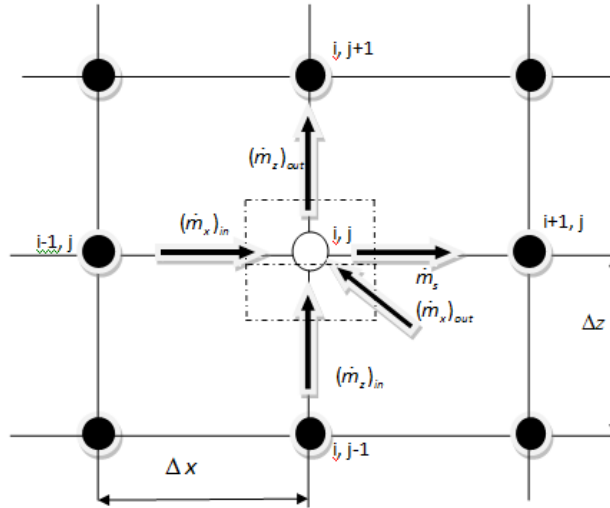


Figure 3.3 Mesh Defined for analysis

Also, \dot{m}_x and \dot{m}_z from the classical formulation of Couette-Poiseuille flows are defined as

$$\dot{m}_x = \left(-\frac{1}{12\mu} \frac{p_j}{R_g T} h_j^3 \frac{\partial p_j}{\partial x} + \frac{p_j}{R_g T} \frac{h_j R \omega}{2} \right) \Delta z \quad (13)$$

$$\dot{m}_z = \left(-\frac{1}{12\mu} \frac{p_j}{R_g T} h_j^3 \frac{\partial p_j}{\partial z} \right) \Delta x \quad (14)$$

In the above equations, x is a local coordinate attached on the bearing surface along the circumferential direction, z is along the axial direction of the bearing, h_j is a film thickness, p_j is pressure, μ is viscosity of air, R_g is the gas constant of air and T is the temperature of the hydrostatic air. The dynamic mass balance of the control volume under transient condition is given by

$$(\dot{m}_x + \dot{m}_z)_{in} + \dot{m}_s - (\dot{m}_x + \dot{m}_z)_{out} = \frac{d(\rho V)}{dx} = \frac{\Delta x \Delta z}{R_g T} \frac{d(p_j h_j)}{dt} \quad (15)$$

where ρ is the density of the supply air and V is the volume of the supply air

Substituting equation (6) and (7) in equation (8), we get,

$$\frac{\partial}{\partial x} \left(-\frac{1}{12\mu} \frac{p_j}{R_g T} h_j^3 \frac{\partial p_j}{\partial x} + \frac{R\omega}{2} p_j h_j \right) + \frac{\partial}{\partial z} \left(-\frac{1}{12\mu} p_j h_j^3 \frac{\partial p_j}{\partial z} \right) + \frac{\partial(p_j h_j)}{\partial t} = \frac{R_g T \dot{m}_s}{\Delta x \Delta z} \quad (16)$$

This is the equation for compressible fluid with hydrostatic air supply

The film thickness of the journal bearing is given by the equation,

$$h_j = C_j - r_{gc} + (e_x + \psi \cdot z) \cos \theta + (e_y - \xi \cdot z) \sin \theta - r_p \cos(\theta - \theta_p) + \delta_j \quad (17)$$

where C_j is a nominal clearance of the journal bearing, r_{gc} is a centrifugal growth of rotor, r_p is a preload distance of each top foil pad, and δ_j is a top foil deflection of journal bearing.

The rotor centrifugal growth is given by following equation. It is considered using the plane stress elastic model, which agree well with the finite element results [25].

$$r_{gc} = \frac{\rho_r r_j \omega^2}{4E} [r_j^2 (1 - \nu)]$$

The top foil deflection of journal bearing follows elastic foundation model combined with 1-D analytical beam model used in [6].

The non dimensionalized Reynolds equation is given by equation(18). Non dimensionalization enables the ease of computation by reducing the number of variables in governing equation. Also non dimensionalization enables us to identify the relative variable from the governing equation. The variables used for nondimensionalization as as shown below

$$P_j = \frac{p_j}{p_a}, Z = \frac{z}{r_j}, \tau = \omega t, H_j = \frac{h_j}{C_j} \text{ and } \Lambda_j = \frac{6\mu\omega}{p_a} \left(\frac{r_j}{C_j} \right)^2$$

$$\frac{\dot{M}_s}{\Delta\theta\Delta Z} + \frac{\partial}{\partial\theta} \left(P_j H_j^3 \frac{\partial P}{\partial\theta} \right) + \frac{\partial}{\partial Z} \left(P_j H_j^3 \frac{\partial P}{\partial\theta} \right) = \frac{\partial}{\partial\theta} (\Lambda_j P_j H_j) + 2\Lambda_j \eta \frac{\partial}{\partial\tau} (P_j H_j) \quad (18)$$

Where $\dot{M}_s = \frac{12\mu R_g T \dot{m}_s}{p_a^2 C_j^3}$

3.2. Experimental Methods

The experimental methods used in determining imbalance response, is discussed in detail in this section. Experiments are carried out at different speeds with the test rig as shown in Figure 2.11. In order to determine the response of a rotor bearing system to calibrated imbalance masses, the rotor should be perfectly balanced without any geometrical tolerance defects. This is not true in practical situation since any every rotor has some residual imbalance present .Manufacturing defects also lead to deviation in rotor geometric tolerances. When rotordynamic measurements are performed, these baseline signals add to the desired calibrated signal. In order to eliminate these baseline signals, baseline subtraction method is adopted.

3.2.1. Baseline Subtraction

In rotordynamic measurement, parasitic featureless baseline signal is superimposed over useful signal from the measured data. In this case, the baseline needs to be subtracted from the measured signal. A process called baseline subtraction is carried out in order to do so.

If system is assumed to behave linearly, imbalance responses follow, such that a linear combination of the imbalance forces results in a net response that may be formed by the linear combination of the responses due to the individual imbalance forces. Similar assumption is applied to our rotor bearing system.

Due to manufacturing defects, the rotor itself carries certain imbalance mass of which location and magnitude are typically difficult to identify. Also the rotor is not perfectly cylindrical. This kind of irregularity produces a response signal, which is called as baseline response. Addition of a known imbalance mass on the rotor at a known location generates total imbalance response. In order to determine the calibrated response of the system to the only known imbalance, the response signals from the baseline imbalance have to be eliminated from the total imbalance response. This method can also be deployed for multiple frequency components i.e. synchronous and other non synchronous frequencies.

Assuming the current system is linear, baseline subtraction method can be applied to two cases.

Case 1: Single frequency component in baseline and total responses + No DC offset
Single frequency component in baseline and calibrated responses + No DC offset
of baseline and calibrated responses is given as

$$\bar{R}_c = \bar{R}_t - \bar{R}_b \quad (19)$$

The response \bar{R} are phasors and are defined by a magnitude and direction (i.e., phase angle)

$$\bar{R} = \bar{R}e^{j\omega t}$$

Where \bar{R} is the phasor comprising of both magnitude and direction

Thus we can write equation (19) as

$$\bar{R}_c e^{j\omega t} = \bar{R}_t e^{j\omega t} - \bar{R}_b e^{j\omega t} \quad (20)$$

Case 2: Multiple frequency components in baseline and total responses + DC offset

$$\bar{R}_c = \bar{R}_t - \bar{R}_b \quad (21)$$

Summing up response of multiple frequency components and DC offset, we have

$$\bar{R}_t = \bar{R}_{t0} + \sum_{k \neq s} R_t^k e^{j\alpha_t^k} e^{j\omega_k t} + R_t^s e^{j\alpha_t^s} e^{j\omega_s t} \quad (22)$$

$$\bar{R}_b = \bar{R}_{b0} + \sum_{k \neq s} R_b^k e^{j\alpha_b^k} e^{j\omega_k t} + R_b^s e^{j\alpha_b^s} e^{j\omega_s t} \quad (23)$$

Where \bar{R}_{b0} and \bar{R}_{t0} are the DC offset from the baseline and total imbalance response, respectively. R_t^k and R_b^k are the response at non synchronous frequency components for total and baseline imbalance response, respectively. R_b^s and R_t^s are the response at synchronous frequencies for baseline and total imbalance response, respectively. ω_s and ω_k are the synchronous and non synchronous frequencies respectively.

Response due to calibrated imbalance is given by the equation

$$\bar{R}_c = \sum_{k \neq s} R_c^k e^{j\alpha_c^k} e^{j\omega_k t} + R_c^s e^{j\alpha_c^s} e^{j\omega_s t} \quad (24)$$

Where R_c^k is the response at non synchronous frequency components and R_c^s is the response at synchronous frequency components

Substituting equation (22) and equation (23) in equation(21), we get

$$\bar{R}_c = \left(\sum_{k \neq s} R_t^k e^{j\alpha_t^k} e^{j\omega_k t} + R_t^s e^{j\alpha_t^s} e^{j\omega_s t} \right) - \left(\sum_{k \neq s} R_b^k e^{j\alpha_b^k} e^{j\omega_k t} + R_b^s e^{j\alpha_b^s} e^{j\omega_s t} \right) \quad (25)$$

Segregating synchronous and non synchronous components, response for synchronous and non synchronous frequency components can be written as

$$R_c^s e^{j\alpha_c^s} = R_t^s e^{j\alpha_t^s} - R_b^s e^{j\alpha_b^s}$$

$$R_c^k e^{j\alpha_c^k} = R_t^k e^{j\alpha_t^k} - R_b^k e^{j\alpha_b^k}$$

In experimentation, we find the baseline and total response at synchronous frequency components and then find the calibrated imbalance response.

$$R_c^s (\cos \alpha_c^s + j \sin \alpha_c^s) = R_t^s (\cos \alpha_t^s + j \sin \alpha_t^s) - R_b^s (\cos \alpha_b^s + j \sin \alpha_b^s) \quad (26)$$

$$R_c^s \cos \alpha_c^s = R_t^s \cos \alpha_t^s - R_b^s \cos \alpha_b^s \quad (27)$$

$$R_c^s \sin \alpha_c^s = R_t^s \sin \alpha_t^s - R_b^s \sin \alpha_b^s$$

$$R_c^s = \sqrt{(R_t^s \cos \alpha_t^s - R_b^s \cos \alpha_b^s)^2 + (R_t^s \sin \alpha_t^s - R_b^s \sin \alpha_b^s)^2} \quad (28)$$

$$\alpha_c^s = \tan^{-1} \left(\frac{R_t^s \sin \alpha_t^s - R_b^s \sin \alpha_b^s}{R_t^s \cos \alpha_t^s - R_b^s \cos \alpha_b^s} \right) \quad (29)$$

3.2.2. Data Process

This section discusses in detail the data processing that is performed on the measured vibration signal. The real time measured signals are consisted of additional frequency components other than the synchronous component. These components may be subsynchronous frequency components and other super synchronous frequency components with small magnitude. These frequency components have to filtered out to obtain a pure synchronous vibration signal. A bandpass Butterworth filter developed by previous researchers [16] was used to extract the synchronous frequency component. Raw rotor vibration data (i.e. time signals) are processed by this digital bandpass filter, which utilizes MATLAB's built-in 'butter' command and a pass band of $\pm 3\%$ of the synchronous frequency. The filtered signals represent the synchronous response of the rotor; however, due to the nature of Digital filtering, the resulting signal is only accurate after a sufficient number of data points have been processed. This filter is supposed to produce accurate results for all rotor speeds above 6000 RPM (100 Hz) from [16].

Accuracy of bandpass filter also depends upon the sampling frequency. The performance of the filter is best at high sampling frequency and its accuracy degrades at lower sampling frequency. In the tests conducted, a sampling frequency of 10000 Hz was used. It was observed that the digital filtering was very efficient up to speeds of 20000 RPM. At speeds greater than that, the filter did not produce pure synchronous components. In order to overcome this, a new digital bandpass Butterworth filter was designed using MATLAB built-in function. The details of the new digital bandpass filter is mentioned in appendix D

Once the filtering of the raw data is performed, the filtered signal was inputted into an in house developed MATLAB code to obtain phase angles and amplitudes at different speed values. This process was performed for baseline, total in phase, and total out of phase imbalance response time signals.

The phase angles and amplitudes obtained from this process are discussed in detail in the next chapter. The calibrated in phase and out of phase imbalance response phase angles and amplitudes are obtained from equation (28) and equation(29).

CHAPTER 4

RESULTS AND DISCUSSIONS

Simulations and empirical tests were performed to determine the imbalance response of the rotor bearing system and their results were compared. These tests were performed in hybrid operation of the AFB. Cylindrical and conical modes of vibrations were excited by applying imbalance masses in the rotor in-phase and out of phase at both ends of the rotor. This chapter discusses the responses of the rotor bearing system for different modes of vibration and also the effect of external supply pressure when the bearing operates in hybrid condition. Table 4.1 shows details of the imbalance mass location and modes of vibration being excited.

Table 4.1 Imbalance mass location and modes of vibration being excited.

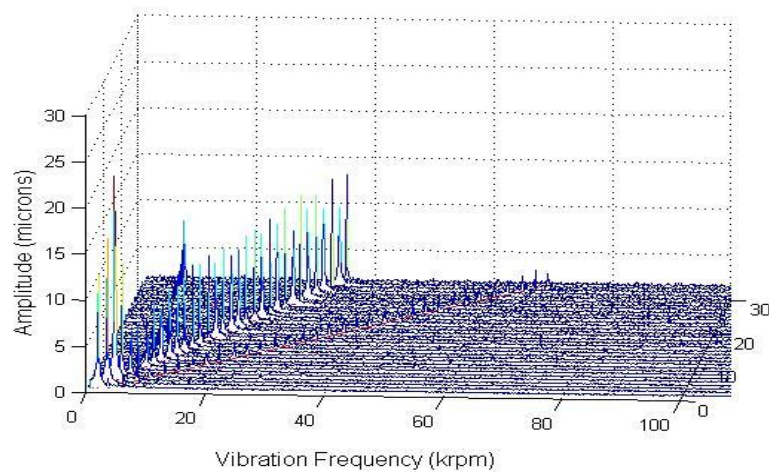
Imbalance mass (mg-mm)	Angular offset of imbalance mass	Mode of Vibration
3800	0°	Cylindrical
3800	180°	Conical

4.1. Imbalance Response in Hydrostatic Mode

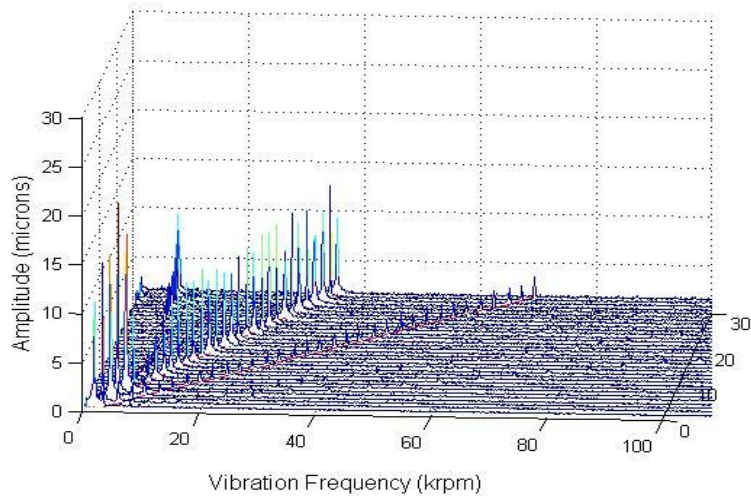
4.1.1. Baseline Response

The rotor consists of some residual imbalance due to manufacturing defects. In order to obtain pure calibrated imbalance response for added imbalance, baseline subtraction method is carried out where calibrated vibration amplitudes and phase angles are determined by subtracting time signal data of added imbalance vibration time signal with the baseline imbalance results. The rotor is run at various speeds to obtain vibration data for residual imbalance. The results are discussed in this section.

Figure 4.1 show the imbalance response of the rotor bearing system due to the residual imbalance present in the rotor. The plots show that the critical speeds along horizontal and vertical direction appear at 3000 RPM and 5000 RPM respectively. This difference in critical speeds arises from the variation in stiffness along horizontal and vertical direction owing to gravitational loading along the vertical direction. Also subsynchronous vibrations appear at speeds of 29000 RPM and become very large at speeds of 34000 RPM.



(a)



(b)

Figure 4.1 Residual Baseline imbalance response waterfall plot. (a) Horizontal direction waterfall plot (b) Vertical direction waterfall plot

Figure 4.2 shows the amplitude curves for various speeds along the horizontal and vertical direction. It is observed that the amplitude along vertical direction is greater than the horizontal direction at critical speed. This phenomenon occurs due to increased stiffness along vertical direction. Figure 4.2 also shows that the critical speed along vertical direction is greater than in horizontal direction. The phase angle plot shows a phase shift at corresponding critical speeds. It is also observed that a local minimum occurs along Horizontal direction amplitude at critical speed of vertical direction. This may be due to the effect of cross coupled stiffness developed within the bearing

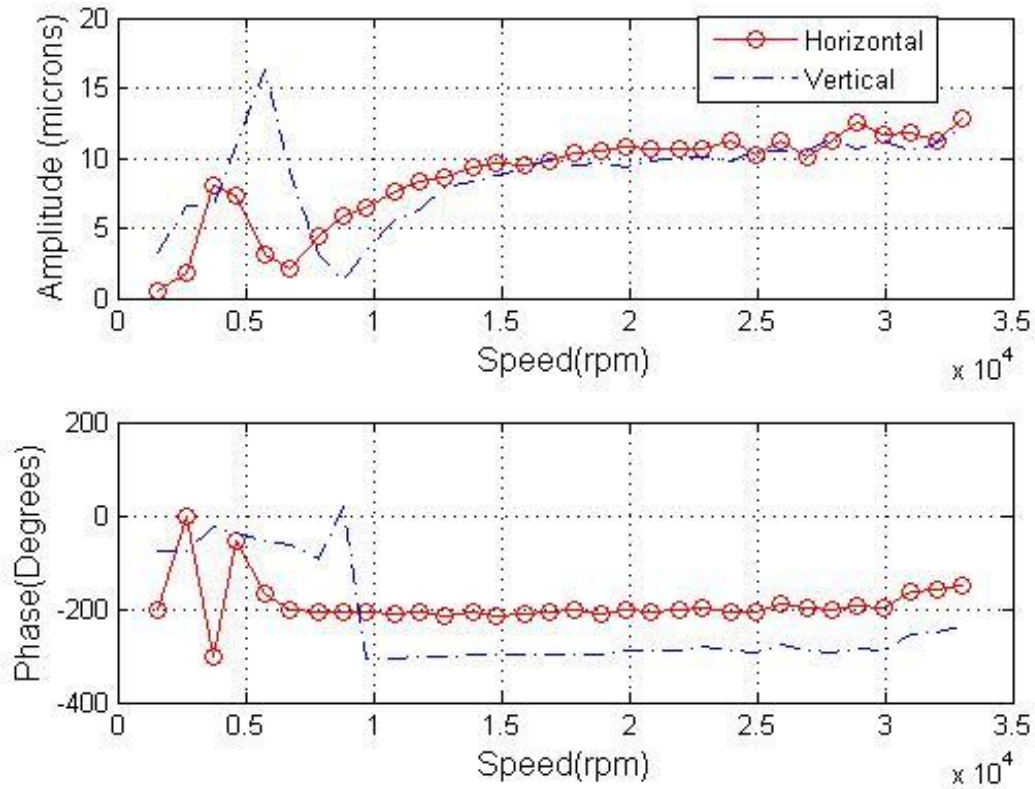
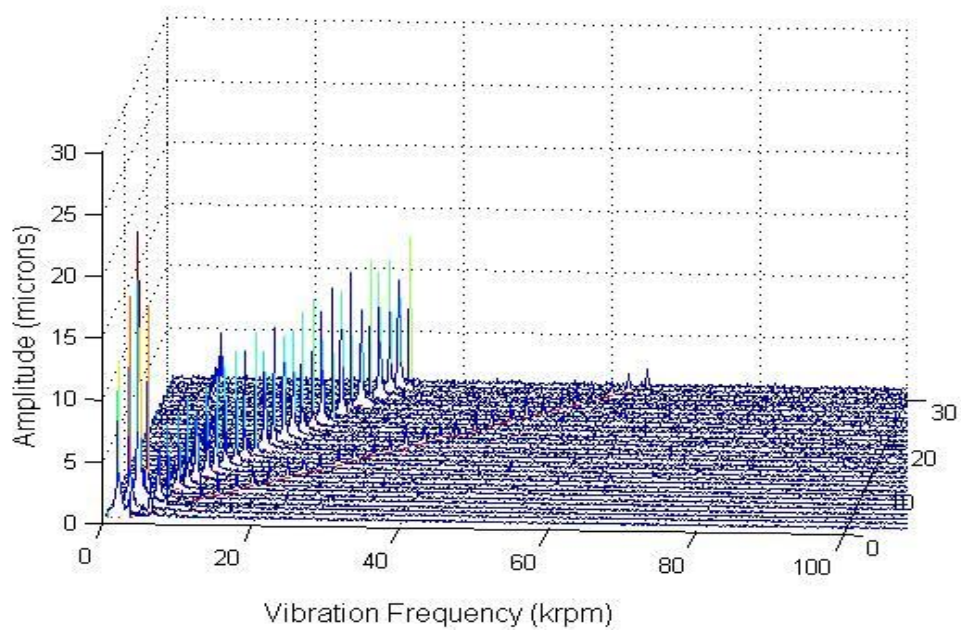


Figure 4.2 Raw Data Bode Plot for baseline vibration along horizontal and vertical direction

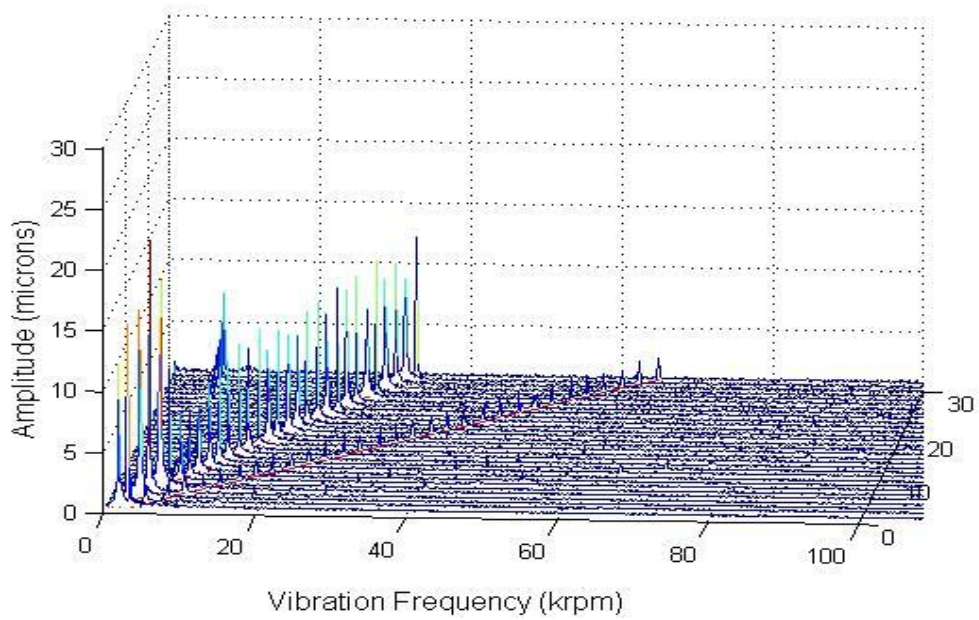
4.1.2. Cylindrical Mode

The rotor imbalances are located at both ends of the rotor with a phase difference of 0° . The journal bearings are located 165 mm away from each other. i.e. $l_b=165\text{mm}$ in figure 3.1. The vibration pick up probes are located 110 mm from the mass center of the rotor. i.e. $l_p=110\text{mm}$ in Figure 3.1. The amount of imbalance added is 3800 mg-mm per bearing. The hydrostatic supply pressure to the journal bearing was maintained at 40psi. Imbalance response tests were performed using the test rig using the same parameters and the results obtained are compared with the simulation results. X direction plots (Gravitational direction) are presented and compared. The results are discussed below.

Figure 4.3 shows the imbalance response of the rotor bearing system when cylindrical mode of vibration is excited in the rotor. The results shown in Figure 4.3 are the response due to added imbalance mass as well as the residual imbalance present in the rotor. It is noticed that subsynchronous vibrations develop at speeds of 29000 RPM. At speeds of 32000 RPM subsynchronous vibrations become too large (amplitudes become greater than synchronous amplitude). Critical speeds are observed at 3000 RPM along the horizontal direction and around 5000 RPM along the vertical. The gravitational loading along the vertical direction renders greater stiffness along the vertical direction. This is the cause for greater critical speeds along the vertical direction. Baseline subtraction method is adopted to determine the calibrated in phase imbalance response of the rotor bearing system.



(a)



(b)

Figure 4.3 Total In Phase imbalance response waterfall plot. (a) Horizontal direction waterfall plot
(b) Vertical direction waterfall plot

Figure 4.4 shows the amplitude curve for cylindrical vibration for varying speeds. Vertical direction is greater than the horizontal direction amplitude by a few microns. Similar to the baseline vibration case, difference in stiffnesses along the vertical and horizontal direction renders different amplitudes at critical speed along horizontal and vertical direction. The phase shift in the phase angle plot indicates the appearance of the critical speed. Also a local minimum is observed along the horizontal direction at 6000 RPM corresponding to local maxima along vertical direction at the same speed. This may be due to the presence of cross coupled stiffnesses arising within the bearing.

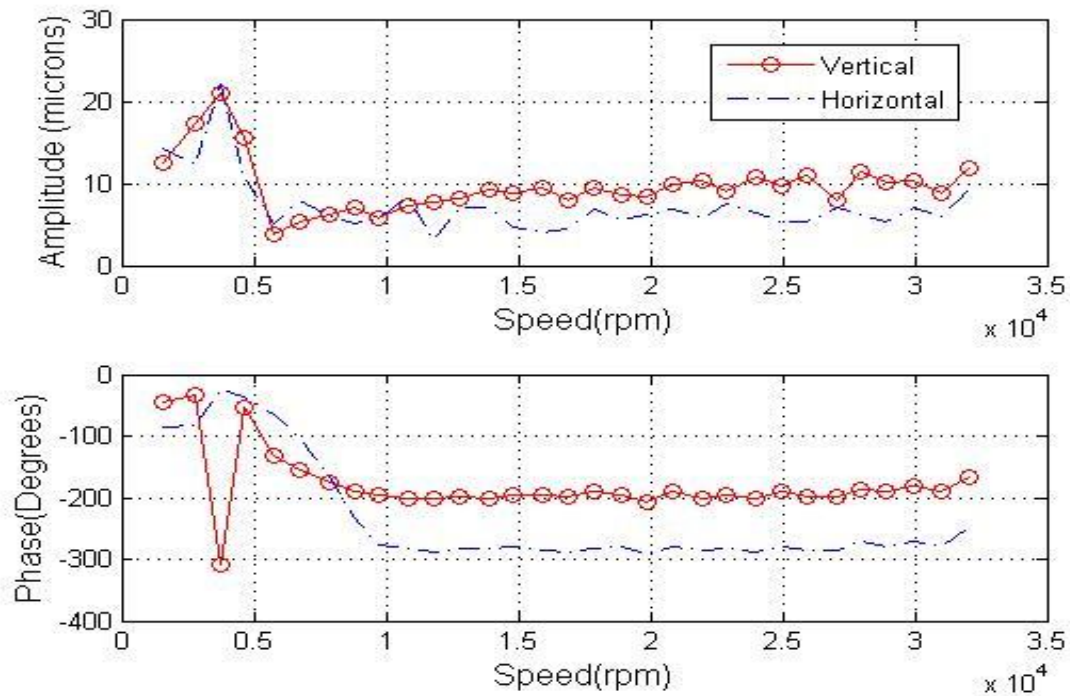


Figure 4.4 Raw Data Bode Plot for cylindrical vibration along horizontal and vertical direction

Figure 4.5 shows the Bode plot of in phase calibrated (Baseline subtracted) amplitude and phase angle cure. It is observed that the critical speed along horizontal and vertical direction appears at speeds of 3000 RPM and 8000 RPM respectively. The phase angle plot also shows a shift in phase at the region of the critical speed. An erratic behavior is noticed in the amplitude and phase angle plot at speeds greater than 20000 RPM. This may be due to the limitation of the

digital bandpass filter which was used during data process of the raw signal. In order to overcome this problem, a new bandpass filter was designed using MATLAB and is discussed in detail in appendix D.

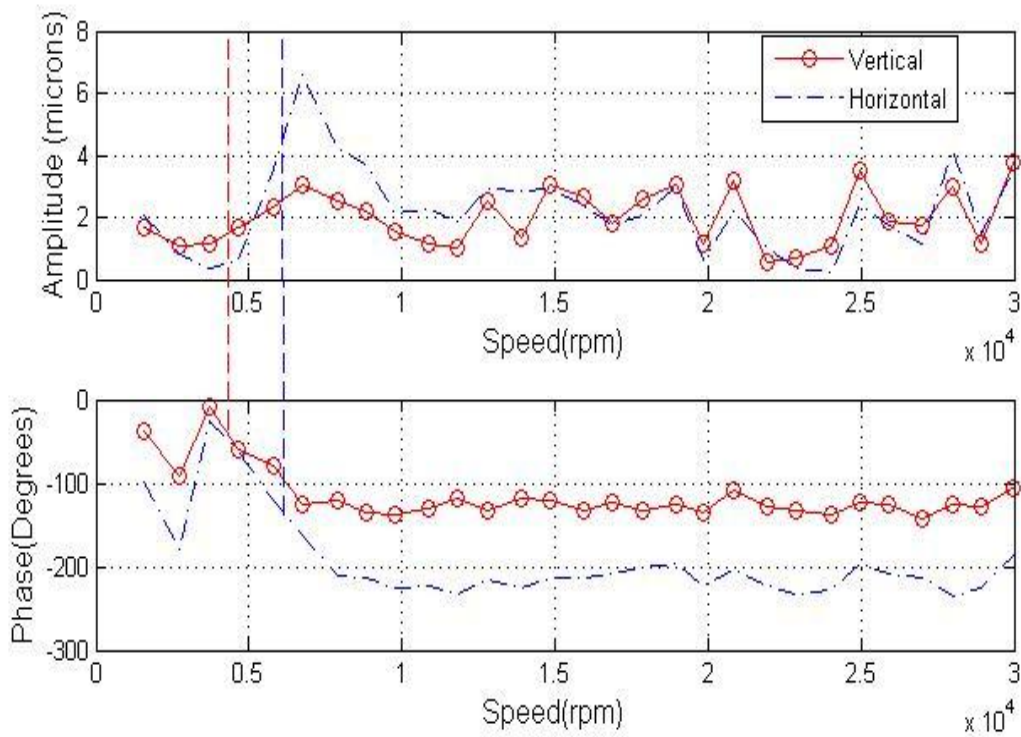


Figure 4.5 Calibrated in phase response amplitude and phase angle curve

Simulations were performed for in phase imbalance response. The effect of thrust bearing was neglected when cylindrical mode of vibration is excited as the thrust forces do not affect the rigid cylindrical mode of vibration. Figure 4.6 show the bode plot for in phase imbalance response. It is observed that the critical speeds, as observed earlier are greater along the gravitational loading direction than in the horizontal direction. Also, small peaks appear along vertical direction at speeds nearing the critical speed of horizontal vibrations and also vice versa. This is due to the effect of cross coupled stiffnesses. The phase angle plot shows a phase shift at critical speeds of corresponding vibration component. At speeds much greater than the critical speed, the amplitude of vibration becomes steady at 3~4 microns.

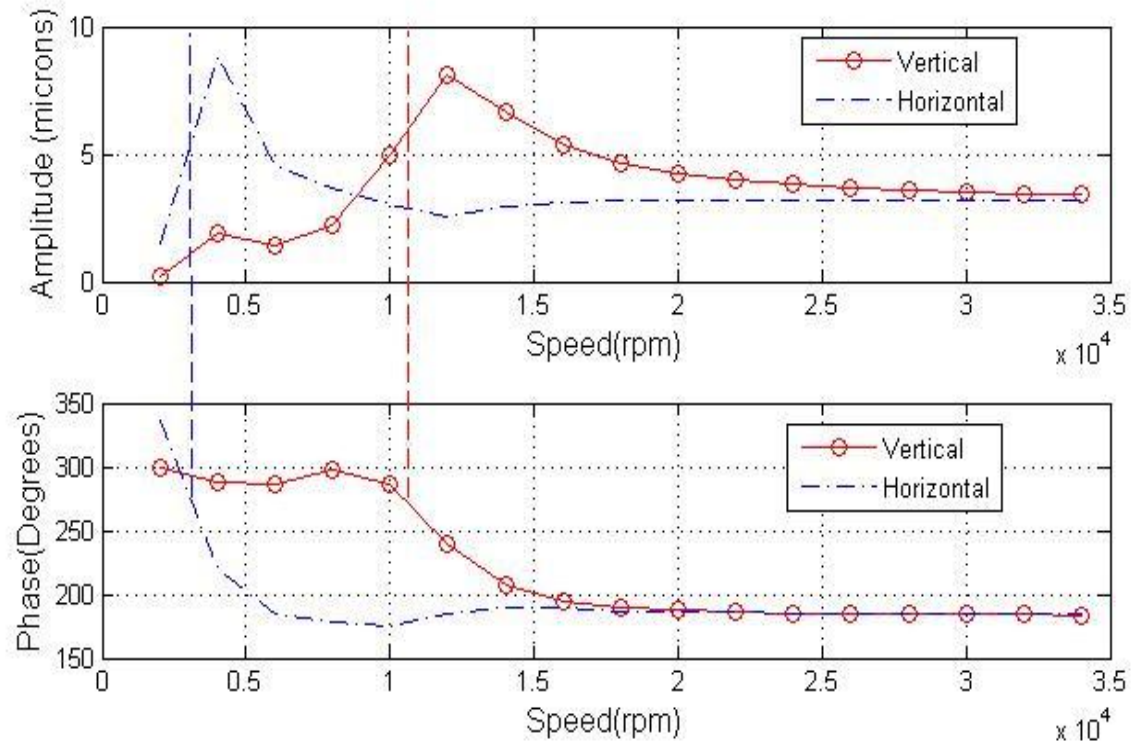
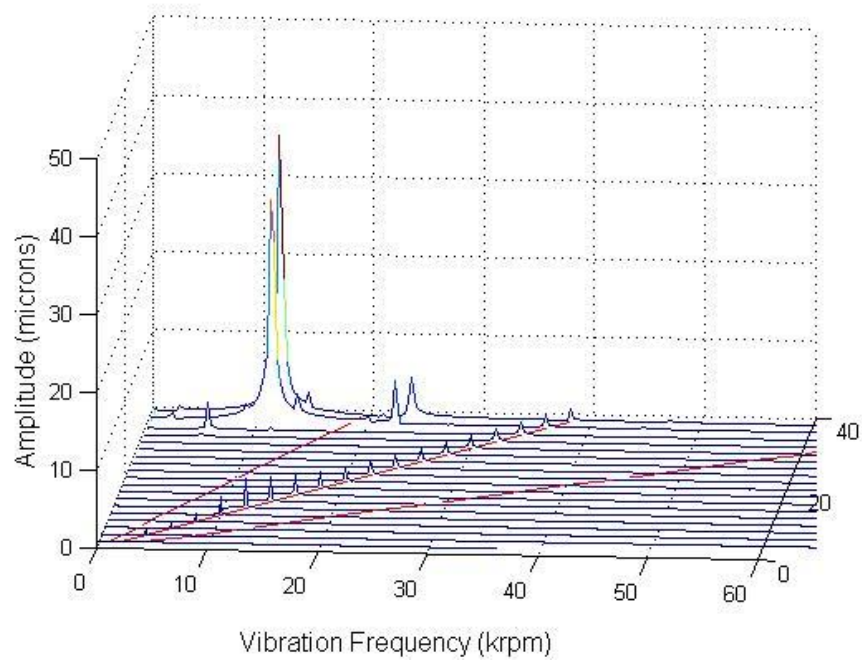
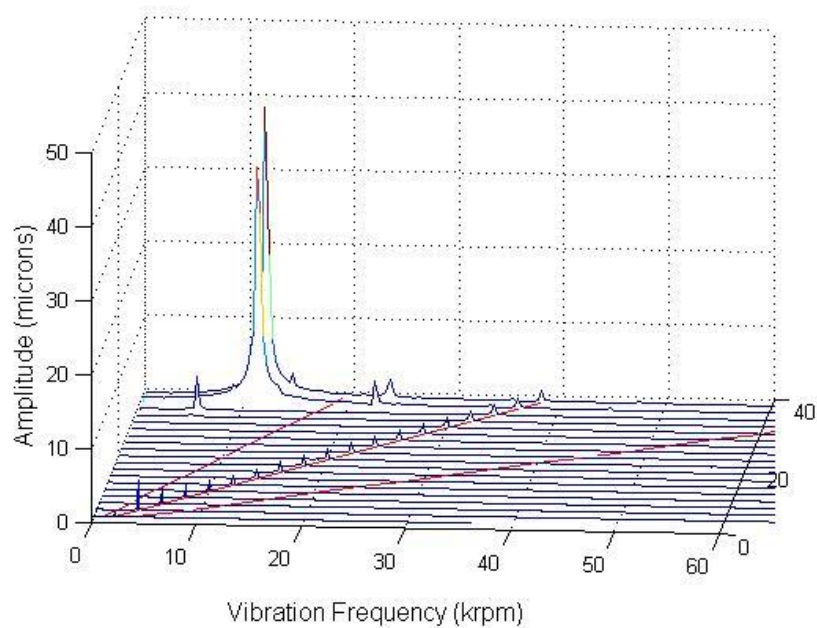


Figure 4.6 Simulation Bode Blot for in phase response

Figure 4.7 shows the waterfall plot for in phase imbalance response obtained from simulations performed using a in house developed Visual C++ code. The plots show that the critical speeds along vertical direction appear at 12000 RPM where as the critical speed along horizontal direction appears at around 3000 RPM. Subsynchronous vibrations are observed at speeds of 32000 RPM which is similar to the results obtained from real time testing. The testing results have a close resemblance with the simulation results in terms of critical speeds and also appearance of subsynchronous vibrations.



(a)



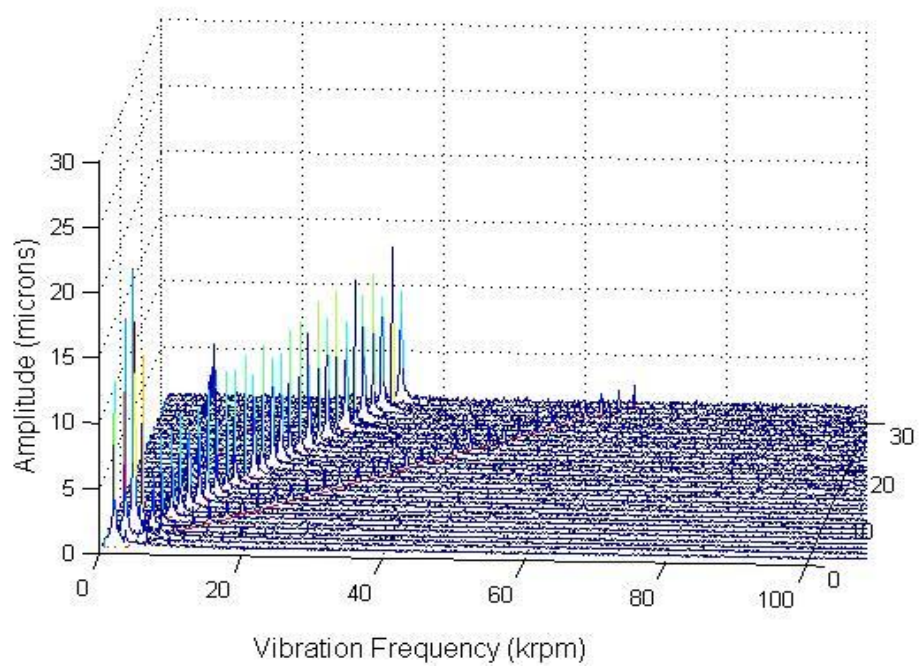
(b)

Figure 4.7 Simulation results- Waterfall plot for in phase imbalance response (a) Vertical Direction(b) Horizontal Direction

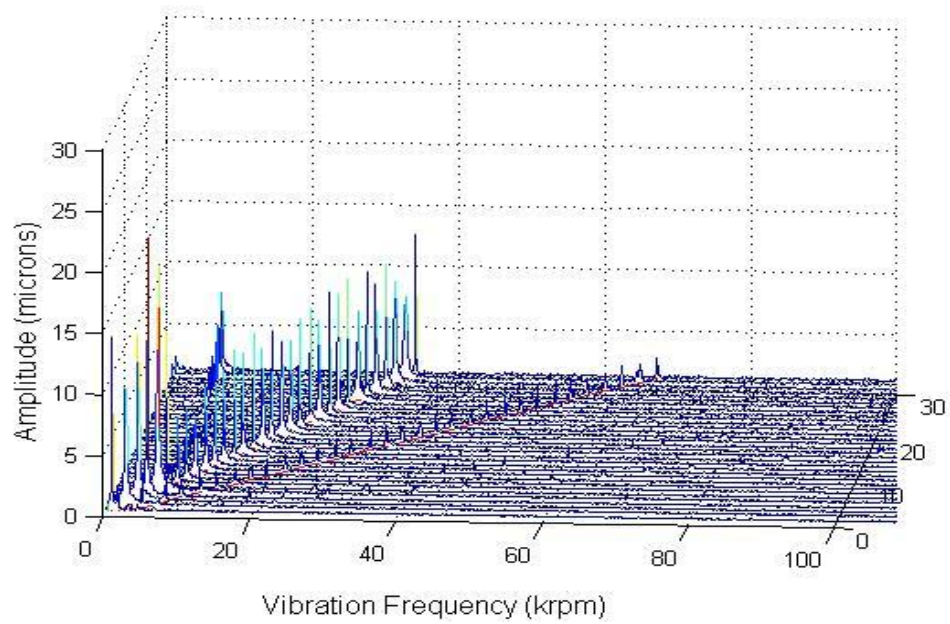
4.1.3. Conical Mode

Conical mode of vibration is excited by applying imbalance mass at both ends of the rotor at an angular phase of 180° . The vibration pick up probes and the bearing locations are same as mentioned in cylindrical mode. The simulation and experimental results are discussed below. Baseline subtraction is also applied to the conical mode and the calibrated out of phase imbalance response of the rotor bearing system is presented in this section.

Figure 4.8 shows the total imbalance response when conical modes of vibration are excited. The response shown in the figures consists of response due to both added imbalance and residual imbalance present in the rotor. It is noticed that critical speed along horizontal direction is appears at speeds of 3000 RPM and along vertical direction is at 5000 RPM. Similar to cylindrical mode, the increase critical speed along vertical direction is due to increased stiffness along the gravitational loading direction. Subsynchronous vibrations are observed at speeds of 29000 RPM. The subsynchronous vibrations showed a rapidly increasing trend at speeds of 33000 RPM with amplitudes greater than synchronous amplitudes. Baseline subtraction is performed to determine the calibrated out of phase imbalance response of the rotor bearing system.



(a)



b)

Figure 4.8 Total out of phase imbalance response waterfall plot (a) Horizontal direction waterfall plot b) Vertical direction waterfall plot

Figure 4.9 shows the amplitude curve for various speed when the rotor is excited to vibrate under conical mode. It is observed that the critical speed (similar to baseline and cylindrical mode) is greater along vertical direction than in horizontal direction. Also the effect of cross coupled stiffness can be observed along horizontal direction amplitudes near the critical speed along vertical direction

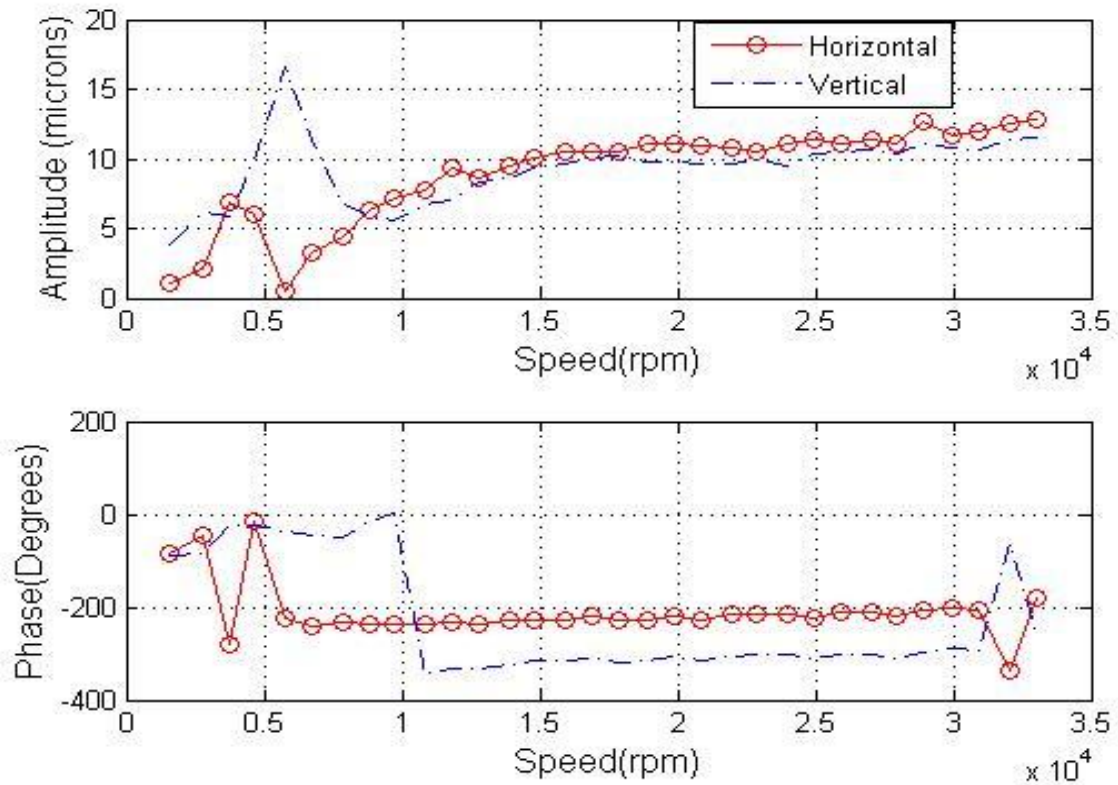


Figure 4.9 Raw Data Speed Vs Amplitude curve for conical vibration along horizontal and vertical direction

Figure 4.10 shows the calibrated out of phase imbalance response Bode plot. The critical speed along vertical direction appears at speeds of 8000 RPM compared to the critical speed along horizontal direction (around 4000 RPM). The amplitude at critical speeds is greater in vertical direction compared to the horizontal direction. The phase angle plot also shows a phase shift indicating appearance of critical speeds. Ineffective filtering causes distortion in the

amplitude and phase angle measurements at speeds of 20000 RPM and above which is clearly observed in the plots.

The rotor bearing system analyzed in this research is a four degree of freedom model. The axial loads (or thrust loads) have not been taken into consideration when imbalance response analysis was made. But thrust forces and moments developed due to thrust load plays a major role in conical mode of vibration. Simulations have not been performed for conical mode of vibration for this reason.

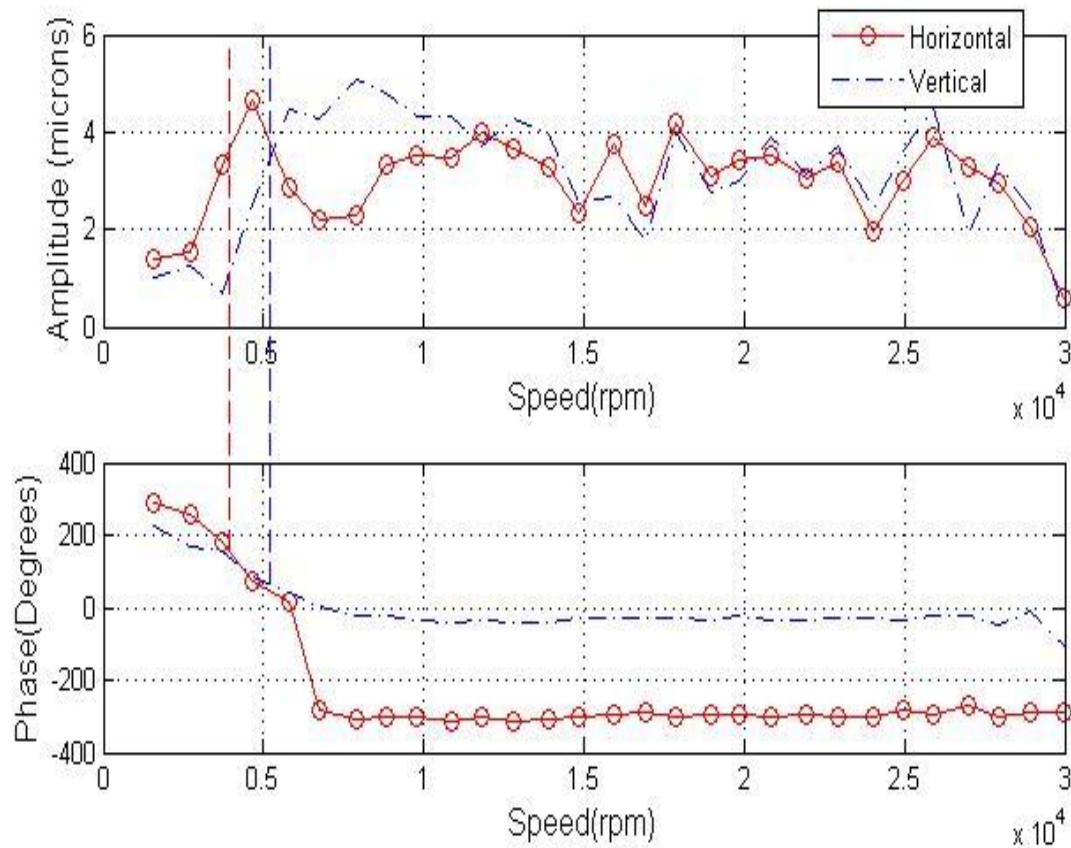


Figure 4.10 Calibrated Out of phase imbalance response Bode Plots

CHAPTER 5

CONCLUSIONS AND RECOMMENDATIONS

5.1. Conclusions

Imbalance response tests were performed at supply pressure of 40 psi by adding in phase and out of phase imbalance of 3800 mg-mm at the two ends of the rotor. Baseline tests were also performed to determine the baseline residual mass response. and then baseline subtraction process was performed to determine the calibrated in phase and out of phase imbalance response. Simulations were also performed to determine the imbalance response for in- phase vibrations. To calculate the rotor motions, dynamic equations of the rotor along with transient Reynolds equation for journal bearing were solved simultaneously.

It is observed that in both cylindrical and conical modes of vibration, the critical speeds along vertical direction are greater than the horizontal direction. This is due to anisotropy of air foil bearings combined with top foil topology. The amplitudes at critical speeds are also greater along vertical direction than in horizontal direction. Effect of cross coupled stiffnesses are also observed at critical speeds along vertical and horizontal direction which is shown by the bode plots for different modes of vibration.

The subsynchronous vibrations were first observed at speeds of 32000 RPM for in phase vibration. But simulation results show that the subsynchronous vibrations remain bounded for speeds as high as 38000 RPM. Testing results showed a similar trend for in phase vibrations. But testing was stopped at speed of 32000 RPM to avoid any damage to the rotor bearing system. The waterfall plots obtained from simulation results also show a close resemblance with the calibrated results with respect to critical speeds and amplitudes at critical speeds. The erratic behavior of amplitudes and phase angles at speeds after critical speeds are due to the inaccuracy of the digital filter used.

Simulations were not performed for out of phase imbalance response as the effect of the thrust bearing were not considered. Thrust forces and the moments due to thrust forces play a major role in out of phase vibration. So it is hard to predict the out of phase vibration response with only a four degree of model system. Calibrated test results follow a similar trend as in-phase vibration with respect to the appearance of critical speeds. Also subsynchronous vibrations were observed at speeds of 32000 RPM but testing was continued until 34000 RPM till a large rise in subsynchronous vibration amplitude was observed. This speed is greater than the speed at which subsynchronous vibrations began to fluctuate for in-phase vibrations (32000 RPM). The distance between journal bearings and the length of the rotor plays a major role in determining the mode of vibration which tends to cause instability. In the case presented in this article, the rotor length and the bearing span are large enough for subsynchronous vibrations due to cylindrical mode to appear first. Thus instability due to cylindrical mode is more dominant than conical vibrations in this case.

5.2. Recommendations for future work

Multiple injection points from the orifice tube:

In this article, the orifice tube used is L shaped and provides only one injection point at the center of the top foil. This results in hydrostatic lift up at the center but may cause rubbing of the rotor with the bearing surface at the edges of the bearing as show in Figure 5.1. To avoid this, a straight orifice tube may be used attached axially along the length of the top foil with more injection points.

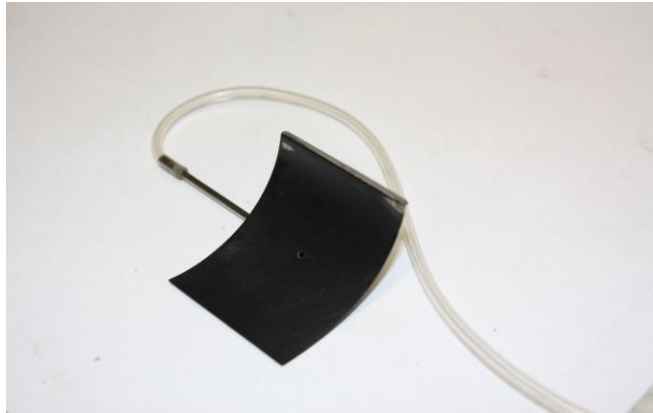


Figure 5.1 Front bearing top foil showing rubbing marks at the edges

Consideration of thrust bearing forces and moments:

Previous researchers [7] have shown that thrust bearing clearance and thrust forces play a major role in imbalance response of a rotor bearing system. A five degree of freedom analysis can be carried out considering the axial thrust load and its effect on in phase and out of phase imbalance response.

Combined cylindrical and conical mode of vibration imbalance response:

This research only deals with cylindrical and conical modes of vibration. A combined cylindrical and conical vibration mode can be excited by adding known imbalances at a phase of 90° at each end of the rotor.

Brazing of orifice tubes on the top foil:

One of the major concerns with soldering the orifice tubes onto the top foil is the strength of the solder at high speeds. Cracks were noticed at the solder joints after tests were run at 32000 RPM, which results in leakage through the top. At much higher speeds, damage to the orifice tube may be catastrophic. In order to avoid this situation, brazing of straight orifice tubes may be adopted on Inconel top foils.

APPENDIX A

SETUP AND OPERATION OF HAFB AND TEST RIG

The section outlines the procedure and instructions for setting up the test rig and also its operation. Also discussed in detail is the procedure to assemble the bearing, alignment of the bearing with rotor, hardware connections and calibration of fiber optic probes.

Bearing Setup and Alignment

As shown in the Figure , the leading edge of the pad has a shorter arc length compared to the trailing edge. Hence, extra care should be taken when assembling the bump foils. Bump foils with smaller flat end region should be assembled along the leading edge side of the pad, so as to avoid interference of this part with lip of the top foil. Small amount of super glue is applied to the lip of the bump foil so as to prevent the sliding motion of the bump foil in the slot. Extra care should be taken to prevent the flow of super glue into the pad region as this would cause interference with the top foil. The edges of the top foil lip are also trimmed in order to prevent any interference with the end plates of the bearing.

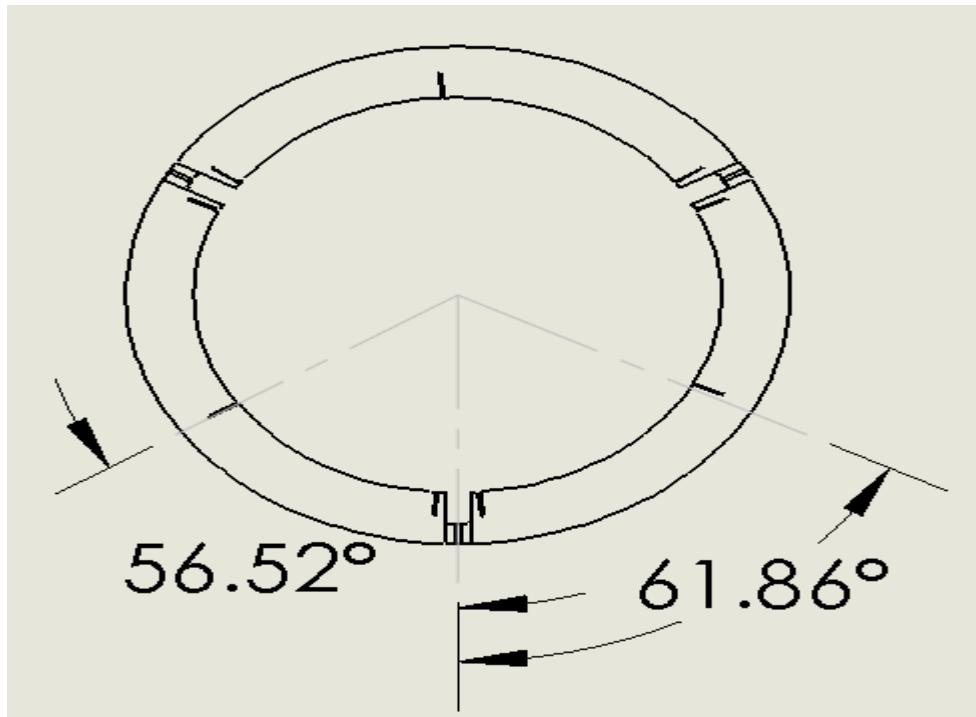


Figure A.1 Bearing housing showing shorter leading edge

Once assembled, there is a minute clearance between rotor and the bearing surface. A hollow cylindrical adapter is designed as an extension to the rotor. The adapter is as shown in Figure A.2 .The adapter with curved edges facilitates easy assembly of the rotor with the bearing without causing any rubbing or damage to the bearing surface. Also, air lines are turned on with air pressures of 40~50 psi during the assembly of the rotor with the bearing.

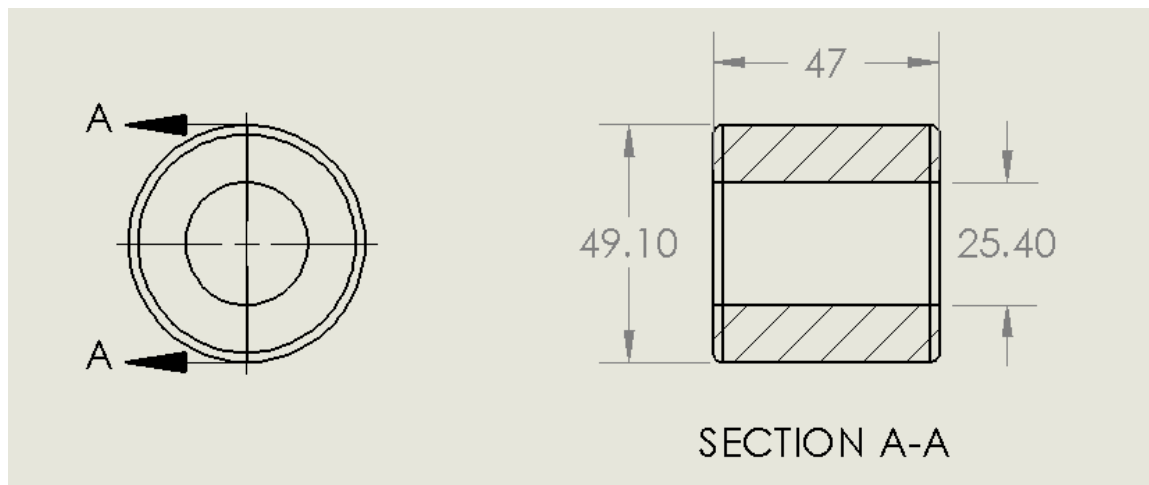


Figure A.2 Schematic of the rotor adapter

The top half of the bearing housing is provided with $\frac{1}{4}$ -20 UNC taps. This taps enables the proper positioning of the bearing and when bolted down, prevents the sliding of the bearing in the housing. The assembly of the HAFB with housing and the rotor is mentioned below

1. The housing is cleaned with acetone and water to prevent any oil or dust remains.
2. The top foils are checked for leakage. The top foils are pressed against the rotor keeping the air line on and liquid soap is sprayed at the joining location of the top foil. Formation of lather gives an indication of the leakage.
3. If no leakage is detected, then the top foils are assembled with the bearing housing by sliding it through the slot while slowly pressing down on the bump foils.
4. Once the bearing is assembled, it is placed in the lower part of the housing and its exact location is determined by matching the tap on the top part of the bearing assembly with the $\frac{1}{4}$ -20 bolt screwed from the top part of the housing.

5. The orifice tubes are pulled out from the front side in case of the front bearing, but in case of the rear bearing, the tubes are pulled out through the slot provided on the lower part of the housing.
6. The top part of the housing is placed on the bottom part by matching the dowel pin holes on the bottom part with the dowel pins attached on the bottom part of the housing.
7. The top part is then screwed to the bottom part, without tightening them too much.
8. The orifice tubes are then connected to the air line and the air pressure is turned on. The air line is then turned on setting the line pressure to about 40 psi.
9. The rotor adapter is then fixed to the front side of the adapter. The rotor is then slid from behind. During the process, the rotor is spun slowly so that the motion of the rotor is smooth.
10. The screws are then tightened to tight.

The thrust bearings are then assembled. The assembly of the thrust bearing is as shown in

Figure A.3

Assembly of Thrust Bearing

Figure A.3 shows the assembly stage of the thrust bearing.

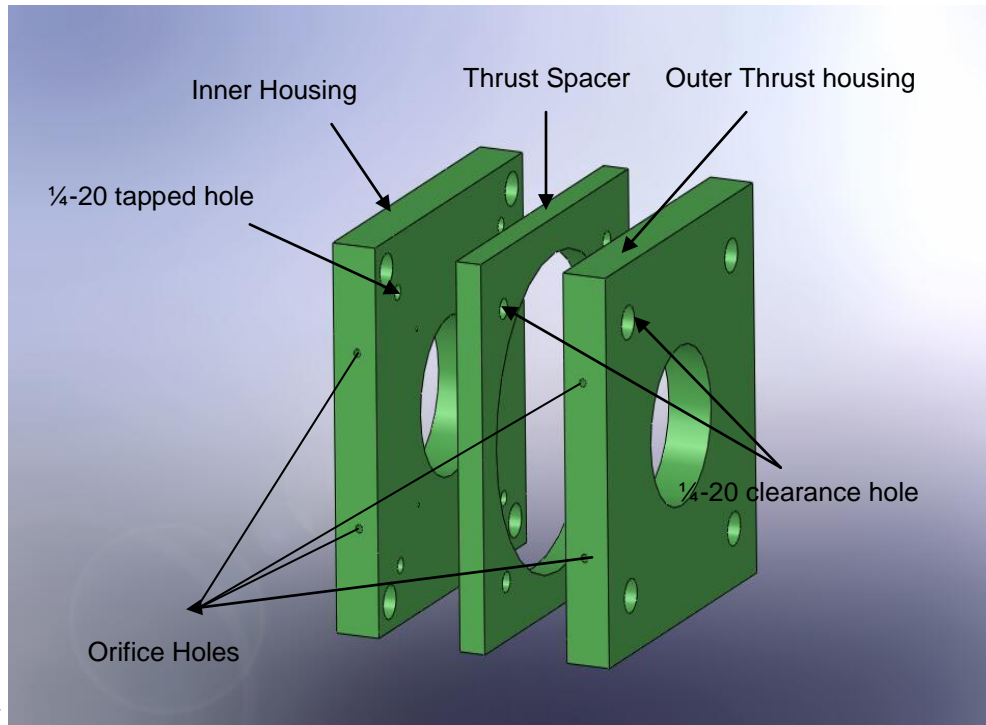


Figure A.3 thrust bearing inner housing, spacer and outer housing exploded view

The assembly procedure is as follows

1. The inner housing is bolted to the journal bearing housing via the 1/4-20 tap holes provided at the rear end of the housing. It is screwed tight to the housing.
2. The spacer and the outer part of the housing is then screwed down to the journal bearing housing though the 1/4-20 counter bore clearance hole provided on the outer housing and the thrust spacer.
3. The inner and outer housing consist of four orifice holes (6-32 tapped holes) at the edges as shown in Figure . The orifice tubes are connected to these holes via orifice connectors. The air line is turned on and line pressure is maintained at 40~50 psi.
4. The inner and outer housing of the thrust bearing have small 3/64 in diameter air supply holes through which the air is supplied to the annulus created by the spacer between the inner and outer part of the housing. These holes are shown in Figure A.4.

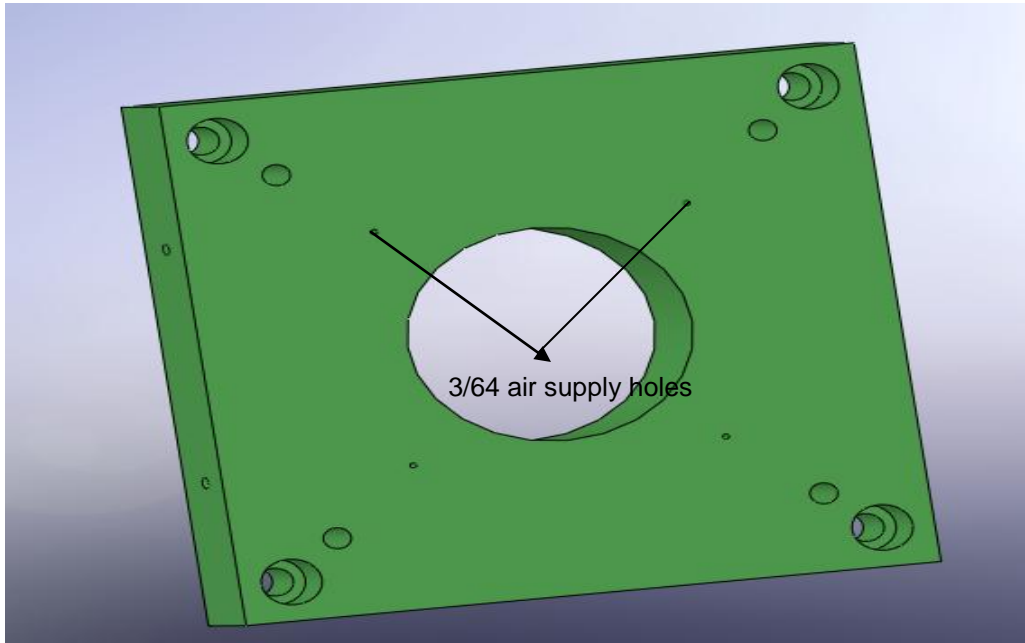


Figure A.4 Outer housing of the thrust bearing showing air supply holes

APPENDIX B

METHOD OF ATTACHING ORIFICE TUBE TO THE BEARING

Manufacturing of Hybrid air foil bearing was a challenge due to the close tolerances and clearances of the bearing. Hybrid air foil bearings demand accurate positioning of the orifice tubes without any leakage of air from the back side of the top foil. Also the alignment of the orifice tubes should be given special attention. Attaching the orifice tubes to the back side of the top foil was achieved though soldering using a Silflo 430 solder for similar metal soldering along with Duzall 430 flux.

Different methods were used to attach the orifice tubes to the top foil. Laser welding was tried initially, but local heating during the process produced some distortions on the bearing surface of the top foil. Though this method eliminated all leakage issues, the slightest protrusion on the top foil surface produced a lot of friction and rubbing on the bearing surface.

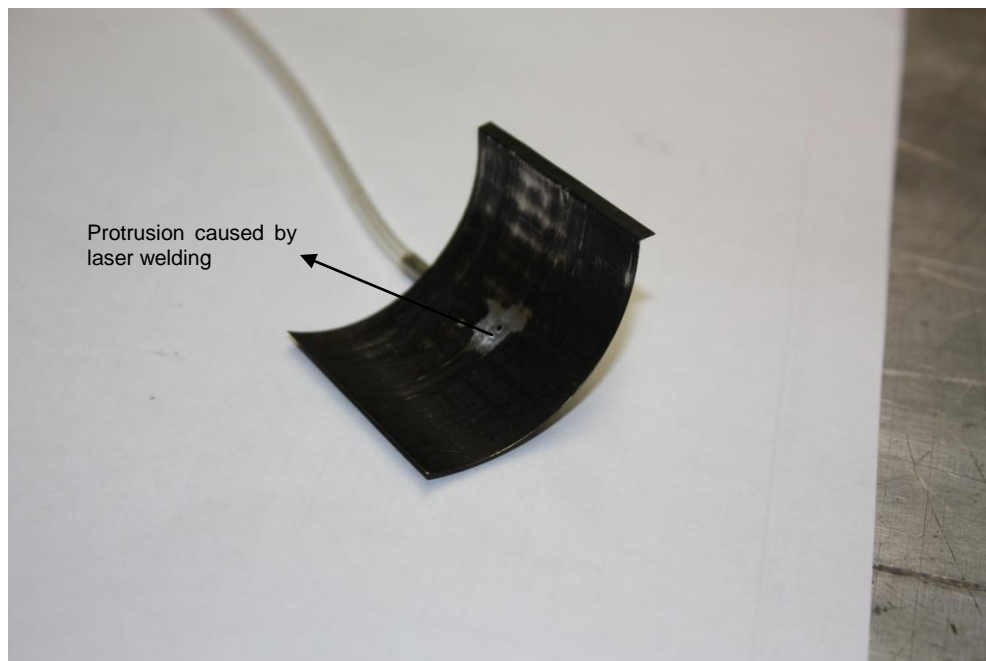


Figure B.1 Top Foils with laser welded orifice tubes showing rubbing marks and protrusion at the air injection area

Brazing of stainless steel tubes on stainless steel top foils was also tried next. The orifice tubes used for brazing had a rectangular cross section. The top foils were to be brazed along the axial length of the top foil. Since the top foil has a curved surface, the orifice tubes never complied with the surface of the top foil. This caused a lot of leakage between the top foil and the

orifice tube. For this reason brazing was discarded. Also brazing process requires heat treatment at temperatures of 1200° F. Stainless steel tends to lose its age hardened properties at this temperature. For these reasons, brazing was not a good method for SS 316 foils.

Soldering was adopted finally to attach the orifice tubes on the top foil. The concern with soldering was to minimize the bead size of the solder (around the orifice tubes) to a minimum to avoid any interference with the bump foils. To achieve a tight hold, considerable amount of solder was applied at the contact surface and the excess solder was then removed by filing it off. Leakage was also a concern with this method, as filing caused some cracks on the soldered section. Solder was applied and filed till no leakage was observed. Strength of the solder to hold the orifice tube is a concern at high speeds. As observed by the Figure , one of the orifice tubes developed cracks after running the tests at 34000 RPM. This leads to leakage from the orifice tubes. Plastic tubing was used as air lines and was attached to the stainless steel orifice tubes using epoxy.



Figure B.2 Front bearing top foil showing crack at the soldered joint

APPENDIX C

DESCRIPTION OF DIGITAL DATA ACQUISITION AND HARDWARE USED

Figure shows the description of the data acquisition system setup adopted from [16]. The equipments numbered in the figure are elaborated in

Table C.1. Further descriptions are also included in the following sections.

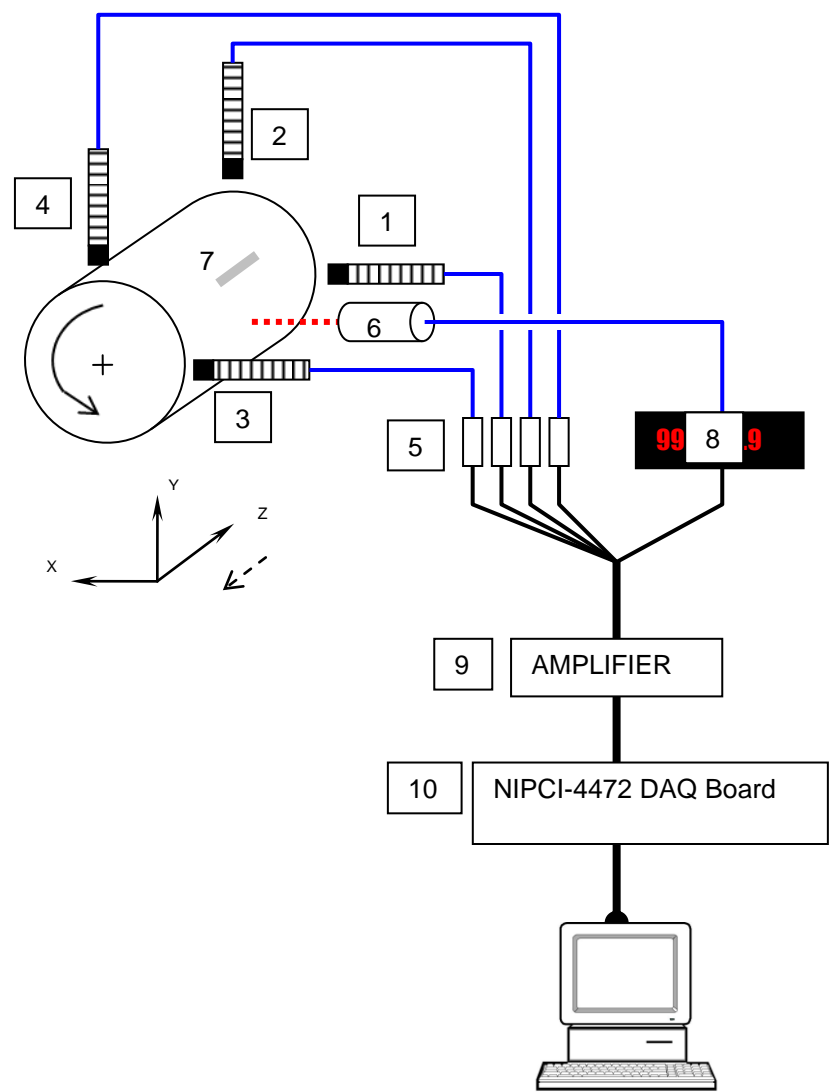


Figure C.1 Schematic of the components used for Data acquisition

Table C.1. Description of hardware used for Data Acquisition

Component Number	Component Name	Description
1	Prox. probe: 'Front-Horizontal'	Bently Nevada 3300 5mm eddy current proximity probes P/N 330171 (1/4-28 UNF threads, without armor).
2	Prox. probe: 'Front-Vertical'	
3	Prox. probe: 'Rear-Horizontal'	
4	Prox. probe: 'Rear-Vertical'	
5	oscillator demodulators	Part of 3300 5mm Proximity Transducer System; uses -24 V dc input
6	Optical or infrared tachometer	Monarch Instrument ROS (Remote Optical Sensor, 1-250.00 krpm range)
7	Tachometer target	ROS requires reflective tape; IRS requires contrasting color (e.g. marker on surface)
8	Tachometer power supply / digital readout	Monarch Instrument ACT-3 Panel Tachometer/Ratemeter/Totalizer;
9	Amplifier	Encore model 517-001 amplifier.
10	Data acquisition (DAQ) board (in PC tower)	National Instruments PCI-4472 dynamic signal board

Proximity Probe wiring and calibration description

The proximity probes used to measure the vibration signal are connected to the amplifier through oscillator demodulator. The wiring description is shown in Figure C.2. Once the connections are made, the probes are calibrated so that they are set up in the bearing housing at their linear range. The calibration details are presented in this section later.

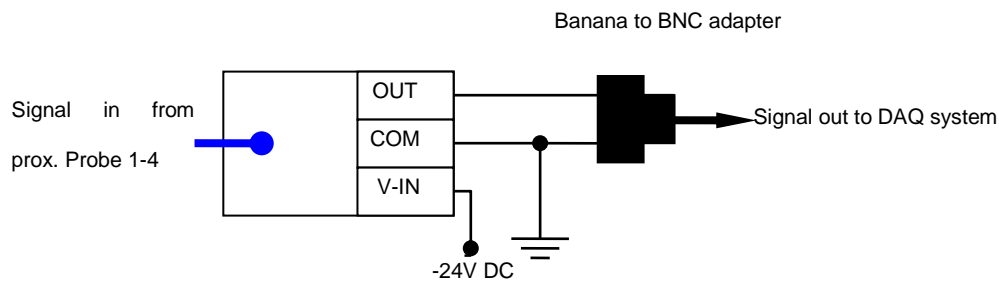


Figure C.2 Probe to Demodulator Wiring Schematic

The probes are connected to the PCI 4472 data acquisition board as shown in the Figure C.2. Once connected, the probes are calibrated with the rotor in position to obtain the linear range of the respective proximity probe. The proximity probes are mounted on a linear stage. The probe is made to touch the rotor using the multimeter. This distance corresponds to distance 0 and the voltage corresponding to this distance is measured. Distance between the rotor and probe is varied using the multimeter and corresponding voltage readings are measured. The voltages are measured over a wide range up to 1 mm. The DC Offset and the gain of the probe is measured and is fed into the National Instruments LABVIEW 8.2 software. Details of the calibration results are shown in Figure C.3 and Table C.3

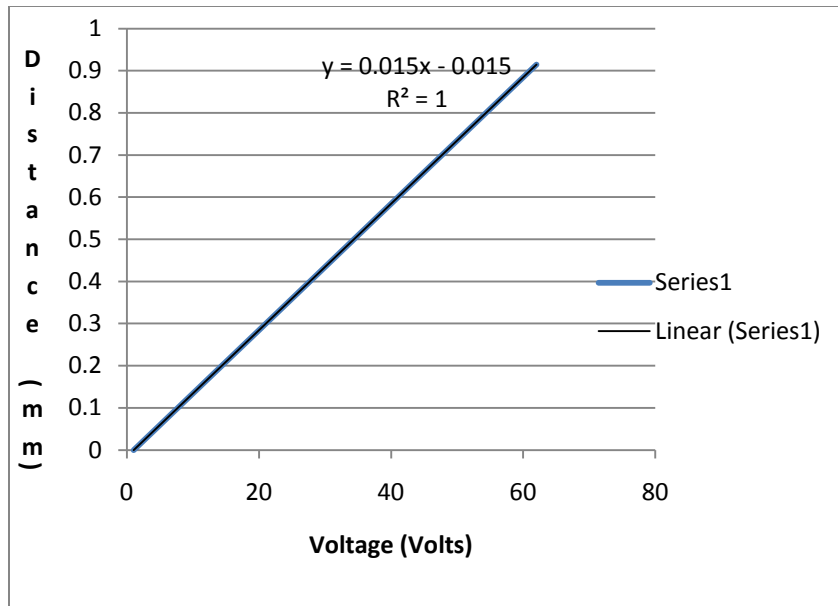


Figure C.3 Probe 1 calibration curve

Table C.2 Linear Range Proximity Probe Calibration Data

Micrometer Reading (Microns)	Voltage (Volts)	distance (Microns)	Gap(Microns)
570	6.482	570	6.482
585	6.659	585	6.659
600	6.836	600	6.836
615	7.019	615	7.019
630	7.196	630	7.196
645	7.37	645	7.37
660	7.546	660	7.546
675	7.718	675	7.718
690	7.904	690	7.904
705	8.082	705	8.082
720	8.262	720	8.262
735	8.44	735	8.44
750	8.619	750	8.619

Proximity probe gains (mV/mm) are found by calibration procedures. Values of proximity probe voltages (post-amplifier voltages) are displayed along with the calculated probe gap (considering net amplifier and proximity probe gains). The gaps may be offset by the user control of 'DC Offset' to set the relative position display to the desired value. Relative position is calculated (with the appropriate unit conversions) by:

$$\text{Rel. pos.} = V_{\text{in}} \frac{1}{G_{\text{probe}}} \frac{1}{G_{\text{amp.}}} + \Delta_{\text{DC offset}}$$

LABVIEW VI Data Acquisition System:

The LABVIEW rotordynamic software was developed previously [16] and was later modified to tap the tachometer key phasor signal. The front panel of the LABVIEW rotordynamic software is as shown in Figure C.4

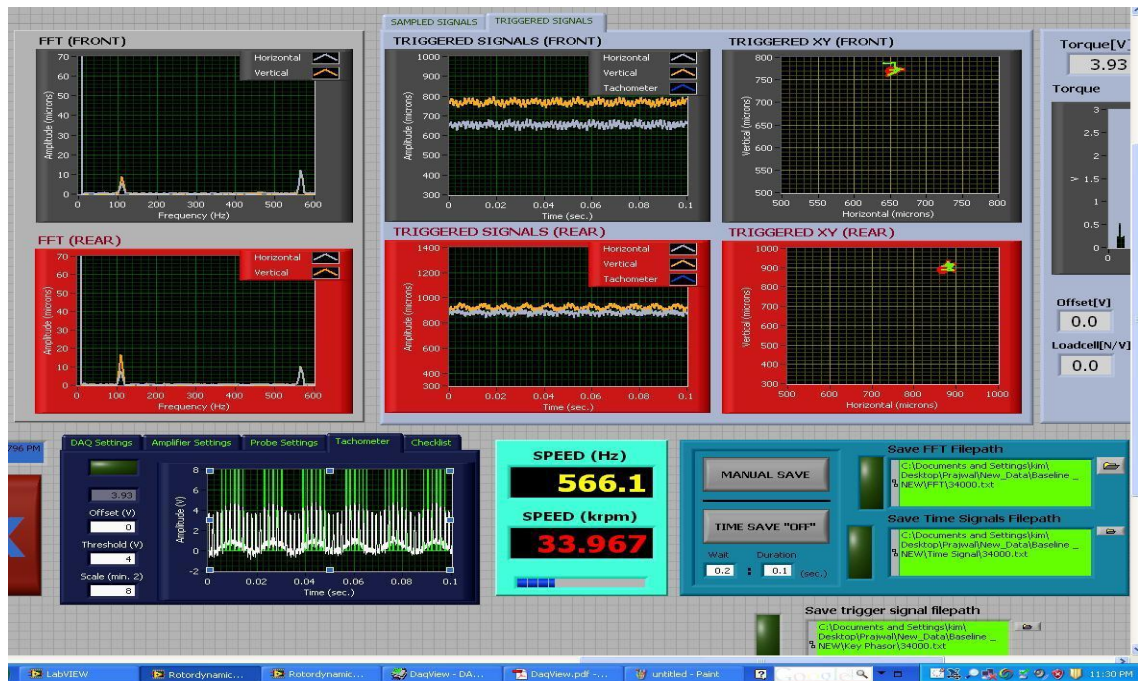


Figure C.4 Front Panel view of Labview Data Acquisition system at 34000 RPM running under Baseline condition

APPENDIX D

LIMITATIONS OF DIGITAL FILTER IMPLEMENTED & DETAILS OF NEW FILTER.

A Bandpass Butterworth type digital filter developed by previous researcher [16] was used for filtering the raw data collected from experimentation. This filter was designed such that the accuracy of filtration depended upon the rotation speed i.e. speeds lower than 6000 RPM had erroneous filtration. Also, due to the nature of the collected raw data, filtering only the synchronous component was tedious task. Also, the filtered time signal shows variation in amplitudes, thereby giving erroneous Bode plots. In order to overcome this problem, a new bandpass Butterworth filter was developed using FDA tools inbuilt function in MATLAB.

The new bandpass filter has a lower cut off frequency and an upper cut off frequency. By limiting the cut off frequency range within the synchronous frequency range, then accurate filtering can be achieved. The accuracy of this filter depends upon the rotor speed recorded by the tachometer. Figure D.1 show the difference in filtering done by the filter used in this research and the newly developed bandpass filter. The sampling frequency used in filtering for both filters in 10000 Hz. The cut of frequency condition for the new digital filter design is as follows.

$$F_{c1} < F_{syn} < F_{c2} \text{ for sampling frequency } F_s = 10000 \text{ HZ}$$

Where F_{c1} = lower cut off frequency

F_{c2} = upper cut off frequency

F_{syn} = Synchronous frequency.

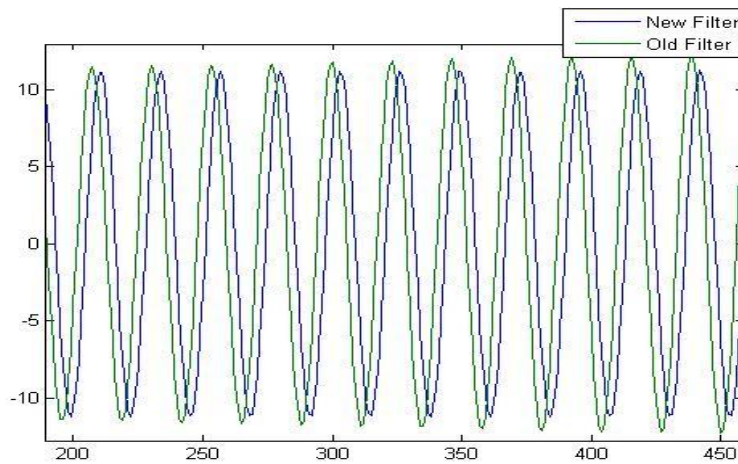


Figure D.1 Filtered signal comparison between the filter used in the article and the new filter designed

It is observed that the filter used in this research has varying amplitudes over time, but the newly designed filter remains steady with amplitude over time. There is a phase shift between the two filtered signals and it has been observed through thorough investigation that the newly developed filter gives more accurate results for amplitude and phase angle for a wide range of speeds.

The following code describes the Filter operations in detail using MATLAB's built in filter command

Function File

```
function Hd = filter_BW

%FILTER_BW Returns a discrete-time filter object.

% M-File generated by MATLAB(R) 7.5 and the Signal Processing Toolbox 6.8.

% Butterworth Bandpass filter designed using FDESIGN.BANDPASS.

% All frequency values are in Hz.

Fs = 10000; % Sampling Frequency

N = 6; % Order

Fc1 = 580; % First Cutoff Frequency

Fc2 = 585; % Second Cutoff Frequency

%DATA = dlmread('1570.txt','t');

%x= (0;2);

% Construct an FDESIGN object and call its BUTTER method.

h = fdesign.bandpass('N,Fc1,Fc2', N, Fc1, Fc2, Fs);

Hd = design(h, 'butter');

% [EOF]
```

Execution File

```
clc, clear all

DATA = dlmread('35030.txt','t');

t = DATA(:,1);
```

```

x = DATA(:,2);
y = DATA(:,3);
speed=35030;
xf=filter_BW;
x_f = filter(xf,x);
yf=filter_BW;
y_f = filter(yf,y);
plot(x);
hold;
plot(x_f);
dlmwrite('17838.xls',[x,y,F,Y_F],'precision','%10.5f'); %generates filtered & unfiltered signal
dlmwrite('25912_1.txt',[t,x_f,y_f],'precision','%10.5f') %generates filtered and unfiltered signal
tau=2*3.1416*speed*t/60;
dlmwrite('32084_FFT.txt',[tau,X_F,Y_F],'precision','%10.5f') % Generates files for FFT Plots
xlim([0 10000])
ylim([-300 5000])

```

BIBLIOGRAPHY

- [1] Agrawal, G. L., 1997, "Foil Air/Gas Bearing Technology -- an Overview," International Gas Turbine & Aeroengine Congress & Exhibition, Orlando, FL, ASME Paper No. 97-GT-347.
- [2] Rubio, D., and San Andrés, L., Bump-Type Foil Bearing Structural Stiffness: Experiments and Predictions, *Journal of Engineering for Gas Turbines and Power*, **Vol.128**(2006), pp. 653-660.
- [3] Kumar, M., and Kim, D., Parametric Studies on Dynamic Performance of Hybrid Air Foil Bearings, *Journal of Engineering for Gas Turbines and Power*, **Vol.130**, No.6(2008), pp. 062501-1-062501-7.
- [4] Heshmat, H., Walowit, J. A., and Pinkus, O., Analysis of Gas Lubricated Compliant Thrust Bearings, *ASME Journal of Lubrication Technology*, **Vol.105**, No.4(1983), pp. 638-646.
- [5] Peng, J. P., and Carpino, M., Calculation of Stiffness and Damping Coefficients for Elastically Supported Gas Foil Bearings, *ASME Journal of Tribology*, **Vol.115**, No.1(1993), pp. 20-27.
- [6] Kim, D., and Park, S., Hydrostatic Air Foil Bearings: Analytical and Experimental Investigations, *Elsevier Tribology International*, **Vol.42**, No.3(2009), pp. 413-425.
- [7] Lee, D., and Kim, D., 2010, "Five Degrees of Freedom Nonlinear Rotor Dynamics Model of a Rigid Rotor Supported by Multiple Airfoil Bearings," Proceedings of the 8th IFToMM International Conference on Rotordynamics, Seoul, Korea, September 12-15.
- [8] Kumar, M., and Kim, D., Static Performance of Hydrostatic Air Bump Foil Bearing, *Elsevier Tribology International*, **Vol.43**, No.4(2010), pp. 752-758, doi:10.1016/j.triboint.2009.10.015.
- [9] Ku, C. -. R., and Heshmat, H., Compliant Foil Bearing Structural Stiffness Analysis: Part I -- Theoretical Model Including Strip and Variable Bump Foil Geometry, *ASME Journal of Tribology*, **Vol.114**, No.2(1992), pp. 394-400.
- [10] Radil, K., Howard, S., and Dykas, B., The Role of Radial Clearance on the Performance of Foil Air Bearings, *STLE Tribology Transaction*, **Vol.45**, No.4(2002), pp. 485-490.
- [11] DellaCorte, C., and Valco, M. J., Load Capacity Estimation of Foil Air Journal Bearings for Oil-Free Turbo-Machinery Applications, *STLE Tribology Transaction*, **Vol.43**, No.4(2000), pp. 795-801.

- [12] Iordanoff, I., Analysis of an Aerodynamic Compliant Foil Thrust Bearing: Method for a Rapid Design, *Journal of Tribology*, **Vol.121**, No.4(1999), pp. 816-822.
- [13] Song, J., and Kim, D., Foil Gas Bearing with Compression Springs: Analyses and Experiments, *ASME Journal of Tribology*, **Vol.129**, No.3(2007), pp. 628-639.
- [14] Kim, D., Parametric Studies on Static and Dynamic Performance of Air Foil Bearings with Different Top Foil Geometries and Bump Stiffness Distributions, *ASME Journal of Tribology*, **Vol.129**, No.2(2007), pp. 354-364.
- [15] D. Kim, A. Lee and Y. Kim, 2008, Hybrid Air Foil Journal Bearings with External Hydrostatic Pressure Supplies, IP disclosure made to University of Texas at Arlington Office of Technology, Reference number 08-60.
- [16] Rimpel, A., and Kim, D., Experimental and Analytical Studies on Flexure Pivot Tilting Pad Gas Bearings with Dampers Applied to Radially Compliant Pads, *ASME Journal of Tribology*, **Vol.131**, No.3(2009), pp.041001(10pages).

BIOGRAPHICAL INFORMATION

Prajwal Shetty received his Bachelor of Engineering degree in Mechanical Engineering from Visveswariah Technological University, India, in May 2007. He is currently pursuing his Master of Sciences degree in Mechanical Engineering at The University of Texas at Arlington, USA. He is a member of the Microturbomachinery and energy Systems Lab, guided by Daejong Kim. His research interests include Rotordynamics, Finite Element Method, Control Systems and design and fabrication with emphasis on Solidworks.